JGR Solid Earth

RESEARCH ARTICLE
10.1029/2023JB028100

A Thermodynamically Based Modified Cam-Clay Model for Post-Bifurcation Behavior of Deformation Bands

Qingpei Sun[1], Xiao Chen[2], Klaus Regenauer-Lieb[3], and Manman Hu[1]

[1]Department of Civil Engineering, The University of Hong Kong, Hong Kong, China, [2]CSIRO Mineral Resources, Australian Resources Research Centre, Kensington, WA, Australia, [3]WA School of Mines: Minerals, Energy and Chemical Engineering, Curtin University, Perth, WA, Australia

Key Points:

- A new thermodynamically consistent Cam-Clay model for deformation bands in porous rocks is presented, alleviating the numerical problem of mesh sensitivity
- The model is based on the modified Cam-Clay plasticity model augmented by an entropic regularization technique, accurately capturing the experimental results for compaction bands in highly porous carbonate
- The mode change from discrete to diffuse post-localisation evolution is found to be related to the reaction-diffusion processes of microstructure interactions

Correspondence to:
M. Hu,
mmhu@hku.hk

Citation:
Sun, Q., Chen, X., Regenauer-Lieb, K., & Hu, M. (2024). A thermodynamically based Modified Cam-Clay model for post-bifurcation behavior of deformation bands. *Journal of Geophysical Research: Solid Earth*, *129*, e2023JB028100. https://doi.org/10.1029/2023JB028100

Received 17 OCT 2023
Accepted 22 FEB 2024

Author Contributions:
Conceptualization: Qingpei Sun, Klaus Regenauer-Lieb, Manman Hu
Formal analysis: Qingpei Sun
Funding acquisition: Klaus Regenauer-Lieb, Manman Hu
Investigation: Xiao Chen
Methodology: Qingpei Sun, Klaus Regenauer-Lieb, Manman Hu
Project administration: Klaus Regenauer-Lieb, Manman Hu
Software: Qingpei Sun
Supervision: Klaus Regenauer-Lieb, Manman Hu
Validation: Qingpei Sun, Xiao Chen
Visualization: Xiao Chen
Writing – original draft: Qingpei Sun, Klaus Regenauer-Lieb, Manman Hu

Abstract Compaction bands are a type of localized deformation that can occur as diffuse or discrete bands in porous rocks. While modeling of shear bands can replicate discrete and diffusive bands, numerical models of compaction have so far only been able to describe the formation of discrete compaction bands. In this study, we present a new thermodynamic approach to model compaction bands that is able to capture both discrete and diffuse compaction band growth. The approach is based on a reaction-diffusion formalism that includes an additional entropy flux. This entropic velocity regularizes the solution, by introducing a characteristic diffusion length scale and controlling the mode change from discrete to diffusive post-localisation growth. The approach is used to model compaction band growth in highly porous carbonates. The model can replicate the areas of material damage exhibiting reduced porosity which are often observed as nuclei for the growth of compaction bands in experiments. The model also has the versatility to predict the formation of diffuse compaction bands, which is a significant advance in the field of compaction band modeling. The method can potentially be used for investigating the effect of material heterogeneities on compaction band growth and is heuristic for developing new methodologies for forecasting compaction band formation.

Plain Language Summary Compaction bands are areas of localized deformation in materials with multiple phases, such as porous rocks. They form when one of the phases localizes and forms bands perpendicular to the direction of the maximum principal effective stress. In this study, we present a new thermodynamically consistent model for compaction bands in porous materials. The model is based on the modified Cam-Clay plasticity model, but it includes a number of additions to make it more realistic and to account for the mesh sensitivity of numerical solutions. We test the new model against experimental results for compaction bands in highly porous carbonate (Mt Gambier limestone). We find that the model can accurately match the experimental results. This new model is a significant advance in the modeling of compaction bands. It has the potential to be used to investigate the effect of material properties, heterogeneity and loading conditions on compaction band formation, and to develop new methods for predicting compaction bands.

1. Introduction

Deformation bands are observed in a wide range of materials resulting from a variety of micro-slips induced by local damage of material, like decohesion, pore collapse, grain crushing, compaction, faulting, nucleation of cavities or sliding on mineral or grain interfaces (Rice, 1976; Rudnicki & Rice, 1975). These local singularities in otherwise homogeneously deforming bodies are appearing as strain localisation in narrow bands and can be modeled by critical conditions in constitutive models for a stationary acceleration wave (Hill, 1962) corresponding to vanishing wave speed of the acoustic tensor (Bigoni & Hueckel, 1991).

The basic theory has been confirmed in numerous numerical and laboratory experimental studies, however, the relation of the macroscopic instability to the micro-slip mechanism causing the material instability is still an unresolved issue. The classical theory does not include microstructural parameters which become important at the onset of localisation. Therefore upon the localisation phenomenon the validity limit of the classical theory is reached and localisation bands of zero-thickness are expected. For the case of a granular material the influence of the microstructure on defining localisation band thickness was shown to be captured by Cosserat theory (Mühlhaus & Vardoulakis, 1987). This led to the formulation of generalized plasticity models by inclusion of higher-order spatial gradients of the plastic strain (Mühlhaus & Aifantis, 1991). More recently probabilistic micromechanics theories have been put forward (Einav & Collins, 2008) providing thermodynamic formulation

Writing – review & editing: Xiao Chen

of the relation between micro-slips and localisation phenomena. Further developments of the theory of thermomechanics are reviewed in (Jacquey & Regenauer-Lieb, 2021) and a robust numerical implementation for rate-dependent critical state line models for damageable materials has been developed (Jacquey, Regenauer-Lieb, & Cacace, 2021). Recently, a phase-field formulation for compaction band formation has been proposed where the physics of grain crushing in high porosity rocks is considered (Ip & Borja, 2022). In this contribution we develop an extension of the damageable rate-dependent critical state line model (Jacquey, Regenauer-Lieb, & Cacace, 2021) by including a reaction-diffusion formalism for modeling the evolution of the microstructure in the localisation band. The numerical models are tested against laboratory results of dynamic evolution of compaction band dynamics in highly porous limestones (Chen et al., 2020a, 2020b).

Compaction bands are defined as narrow, tabular strain localisation features that form perpendicular to the direction of maximum compressive stress (Baxevanis et al., 2006; Chemenda, 2009). Analytical and numerical solutions following the classical theory of localisation (Rudnicki & Rice, 1975) for a Drucker-Prager constitutive model showed that the ratio between the band thickness and the band-to-band distance is related to the constitutive and stress-state parameters (Chemenda, 2009). In particular the hardening modulus and dilatancy factor were found to have a first order influence on the spacing of the bands. The lack of an internal length scale in the classical models is often apparent through mesh-dependency of the numerical models. The usefulness of the approach applied to interpret the fault network structures observed in the field was illustrated in (Chemenda et al., 2014), however, the mesh sensitivity problem remained an open issue.

In this contribution we explore a new strategy for the numerical formulation inspired by closed-form analytical solutions of compaction band formation for porous media with a nonlinear power-law viscous reactive source term stemming from the deformation of the solid matrix (Alevizos et al., 2017; Veveakis & Regenauer-Lieb, 2015). The formulation reproduces the results of Terzaghi's consolidation theory for highly permeable rocks with a low ratio of solid over fluid pressure diffusivities. At a critical ratio ($\gtrapprox$13) the solution becomes singular and a compaction band nucleates. For higher ratios, the number of compaction bands is expected to increase. The analytical solution was found to share the same problem of being unable to predict the band width as in the classical theories. In the follow-up numerical experiments, the width of the bands can be regularized through considering the internally induced chemical reactions (Alevizos et al., 2017). We generalize this consideration of reaction rates in the current work to regularize the evolution of the damage variable via the dynamic renormalization of a reaction-diffusion formalism at long time scales.

In the following we will recap the previous formulation in (Jacquey & Regenauer-Lieb, 2021) in the context of the classical acoustic tensor theory and proceed with a proposed extension to regularize the width of the deformation bands through considering the dynamic evolution of the localisation bands described by the reaction-diffusion approach. A thermodynamic approach based on an application of Onsager's reciprocacy assumption for nonlocal, damageable rheology was introduced in (Lyakhovsky et al., 2011), which relates the width of the localized zone to damage diffusion as well as the off-fault damage to the efficiency of the damage-diffusion process (Kurzon et al., 2021). In this work we generalize the approach by introducing a characteristic entropic velocity, obtained from a relaxation of Onsager's local equilibrium assumption for nonlocal damage processes (Regenauer-Lieb & Hu, 2023). The focus of the current work is hence on developing a self-consistent thermodynamic model that is capable of investigating the dynamics of the post-localisation regime where higher order strain gradients need to be considered. The nonlocal approach incorporates the effects of microstructure on the macroscopic behavior of materials in continuum mechanics. The key idea we adopt is that the stress at a point in a material depends not only on the strain at that point, but also on the strains at neighboring points (Triantafyllidis & Aifantis, 1986). Consequently, we develop the mathematical and numerical model and go on to test whether the model captures the rich dynamic field of post-localisation evolution of compaction band formation revealed in experiments with highly porous limestones (Chen et al., 2020a, 2020b). After demonstrating the capability of the dynamically renormalized thermomechanics approach, alleviating the long-lasting mesh dependency issue, we proceed to discuss the potential of the proposed model as well as the limitations.

2. Theoretical and Numerical Models

2.1. Modified Cam-Clay (MCC) Model for Damageable Elasto-Plastic Materials

2.1.1. Elasto-Plastic Materials

For elasto-plastic materials subject to external loading, the rate of work $\hat{W}$ can be expressed via the double inner product of Cauchy stress $\boldsymbol{\sigma}$ and the total strain rate $\dot{\boldsymbol{\varepsilon}}$ following

$$\hat{W} = \boldsymbol{\sigma} : \dot{\boldsymbol{\varepsilon}} = \dot{\Psi} + \hat{\Phi}, \quad \hat{\Phi} \geq 0 \tag{1}$$

where $\dot{\Psi}(\boldsymbol{\varepsilon}, \boldsymbol{\xi}) = \frac{\partial \Psi}{\partial \boldsymbol{\varepsilon}} : \dot{\boldsymbol{\varepsilon}} + \frac{\partial \Psi}{\partial \boldsymbol{\xi}} : \dot{\boldsymbol{\xi}}$ is the rate form of Helmholtz free energy, and $\hat{\Phi}$ denotes the dissipation rate, with the notation $\hat{\cdot}$ representing the rate form of a non-state function. Here, $\boldsymbol{\xi}$ is an internal variable, which is a tensorial strain-like quantity (Houlsby & Puzrin, 2007). For materials whose elastic moduli are independent of the plastic deformation, that is, the so-called "decoupled materials," the internal variable in such cases can be identified as the plastic strain $\boldsymbol{\varepsilon}^p$ (Collins & Houlsby, 1997), which results in

$$\dot{\boldsymbol{\varepsilon}} = \dot{\boldsymbol{\varepsilon}}^e + \dot{\boldsymbol{\varepsilon}}^p, \quad \dot{\boldsymbol{\varepsilon}}^p = \dot{\boldsymbol{\xi}} \tag{2}$$

Equation 2 shows the additive decomposition of the strain rate tensor based on thermodynamics principles, which is commonly assumed in elasto-plastic theories. In the following, we mainly focus on "decoupled materials," and the introduction about "coupled materials" can be found in the relevant literature (Collins, 2002). Like the splitting of strain rate tensor, the Helmholtz free energy for the "decoupled" case can also be decomposed additively into two parts as

$$\Psi(\boldsymbol{\varepsilon}, \boldsymbol{\xi}) = \Psi^e(\boldsymbol{\varepsilon}^e) + \Psi^p(\boldsymbol{\varepsilon}^p) \tag{3}$$

where $\Psi^e(\boldsymbol{\varepsilon}^e)$ is the elastic Helmholtz free energy depending on the elastic deformation and $\Psi^p(\boldsymbol{\varepsilon}^p)$ is the plastic Helmholtz free energy depending on the plastic strain. For rate-independent elasto-plastic materials, the dissipation function is homogeneous of degree 1 in the internal variable rate $\dot{\boldsymbol{\xi}}$ with the use of Euler's theorem (Zhao et al., 2006), and $\hat{\Phi}$ can be expressed as

$$\hat{\Phi} = \frac{\partial \hat{\Phi}}{\partial \dot{\boldsymbol{\xi}}} : \dot{\boldsymbol{\xi}} = \frac{\partial \hat{\Phi}}{\partial \dot{\boldsymbol{\varepsilon}}^p} : \dot{\boldsymbol{\varepsilon}}^p \tag{4}$$

Substituting Equations 2–4 into Equation 1, leads to

$$\hat{W} = \boldsymbol{\sigma} : \dot{\boldsymbol{\varepsilon}}^e + \boldsymbol{\sigma} : \dot{\boldsymbol{\varepsilon}}^p = \dot{\Psi}^e + \dot{\Psi}^p + \hat{\Phi} = \frac{\partial \Psi^e}{\partial \boldsymbol{\varepsilon}^e} : \dot{\boldsymbol{\varepsilon}}^e + \frac{\partial \Psi^p}{\partial \boldsymbol{\varepsilon}^p} : \dot{\boldsymbol{\varepsilon}}^p + \frac{\partial \hat{\Phi}}{\partial \dot{\boldsymbol{\varepsilon}}^p} : \dot{\boldsymbol{\varepsilon}}^p \tag{5}$$

from which we can deduce that.

$$\boldsymbol{\sigma} = \frac{\partial \Psi^e}{\partial \boldsymbol{\varepsilon}^e} \tag{6a}$$

$$\boldsymbol{\sigma} = \frac{\partial \Psi^p}{\partial \boldsymbol{\varepsilon}^p} + \frac{\partial \hat{\Phi}}{\partial \dot{\boldsymbol{\varepsilon}}^p} = \boldsymbol{\varrho} + \boldsymbol{\chi} \tag{6b}$$

With the shift stress $\boldsymbol{\varrho}$ and dissipative stress $\boldsymbol{\chi}$ defined respectively as

$$\boldsymbol{\varrho} = \frac{\partial \Psi^p}{\partial \boldsymbol{\varepsilon}^p} \tag{7}$$

$$\boldsymbol{\chi} = \frac{\partial \hat{\Phi}}{\partial \dot{\boldsymbol{\varepsilon}}^p} \tag{8}$$

Equation 6a allows to recover the Hooke's law of elasticity by considering the following elastic Helmholtz free energy

$$\Psi^e(\boldsymbol{\varepsilon}^e) = \frac{1}{2}K\left(\varepsilon_v^e\right)^2 + \frac{3}{2}G(\gamma^e)^2 \tag{9}$$

where K and G are the bulk modulus and the shear modulus, respectively, $\varepsilon_v^e = -\varepsilon_{kk}^e$ and $\gamma^e = \sqrt{\frac{2}{3}\boldsymbol{e}^e : \boldsymbol{e}^e}$ the volumetric and shear elastic strain invariants, respectively, with $\boldsymbol{e}^e = \boldsymbol{\varepsilon}^e + \frac{1}{3}\varepsilon_v^e \boldsymbol{I}$ denoting the elastic deviatoric strain tensor, and $\boldsymbol{I}$ representing the second-rank identity tensor. The elastic stress-strain relationship is thus expressed as

$$\sigma_{ij} = \mathbb{C}_{ijkl} : \varepsilon_{kl}^e, \quad \mathbb{C}_{ijkl} = K\delta_{ij}\delta_{kl} + G\left(\delta_{ik}\delta_{jl} + \delta_{il}\delta_{jk} - \frac{2}{3}\delta_{ij}\delta_{kl}\right) \tag{10}$$

where $\mathbb{C}$ is the elasticity tensor and δ the Kronecker delta. Equation 6b shows a fundamental relation in the thermodynamics theory, which relates the true stress tensor (i.e. Cauchy stress $\boldsymbol{\sigma}$) to the shift stress tensor $\boldsymbol{\varrho}$ and the dissipative stress tensor $\boldsymbol{\chi}$. The shift stress $\boldsymbol{\varrho}$ is associated with the hardening (including softening) of the material when the center of the yield function moves in the true stress space, and the dissipative stress $\boldsymbol{\chi}$ is related to plastic dissipation during loading. This decomposition of the true stress allows to formulate the yield function and the flow rule in the dissipative stress space where non-trivial description of strain localisation ranging from compaction bands to shear-enhanced compaction bands under different confining pressure can be captured, using a relatively simple mathematical expression of the yield function.

In what follows, we present the thermodynamic derivation of a general family of critical state line models which are commonly used for localisation study. Following (Collins, 2003; Collins & Kelly, 2002), the dissipation function for critical state models can be expressed as

$$\hat{\Phi} = \sqrt{\left(A\dot{\varepsilon}_v^p\right)^2 + \left(B\dot{\gamma}^p\right)^2} \tag{11}$$

where the coefficients A and B are associated with the true pressure $p = -\sigma_{kk}/3$ and the consolidation pressure p_c

$$A = (1-\gamma)p + \frac{1}{2}\gamma p_c, \quad B = \mu\left[(1-\alpha)p + \frac{1}{2}\alpha\gamma p_c\right] \tag{12}$$

and $\dot{\varepsilon}_v^p$ and $\dot{\gamma}^p$ are the rate of the plastic volumetric and shear strain invariants. The introduction of the consolidation pressure provides a way to account for both plastic dilation and compression at different stress states while the classical frictional formulation only considers the plastic dilation. Note that α and γ in Equation 12 are two dimensionless coefficients smaller than one and μ is a dimensionless constant representing the friction of the material. As the stress is usually decomposed into the mean effective and deviatoric parts for the analysis of localisation problems, the dissipative stress in Equation 8 is similarly formulated as

$$\pi = \frac{\partial\hat{\Phi}}{\partial\dot{\varepsilon}_v^p} = \frac{A^2\dot{\varepsilon}_v^p}{\hat{\Phi}}, \quad \chi = \frac{\partial\hat{\Phi}}{\partial\dot{\gamma}^p} = \frac{B^2\dot{\gamma}^p}{\hat{\Phi}} \tag{13}$$

where π is the dissipative pressure and χ is the dissipative deviatoric stress. Rearranging Equation 13 and substituting into Equation 11 give rise to

$$\hat{\Phi} = \hat{\Phi}\sqrt{\frac{\pi^2}{A^2} + \frac{\chi^2}{B^2}} \tag{14}$$

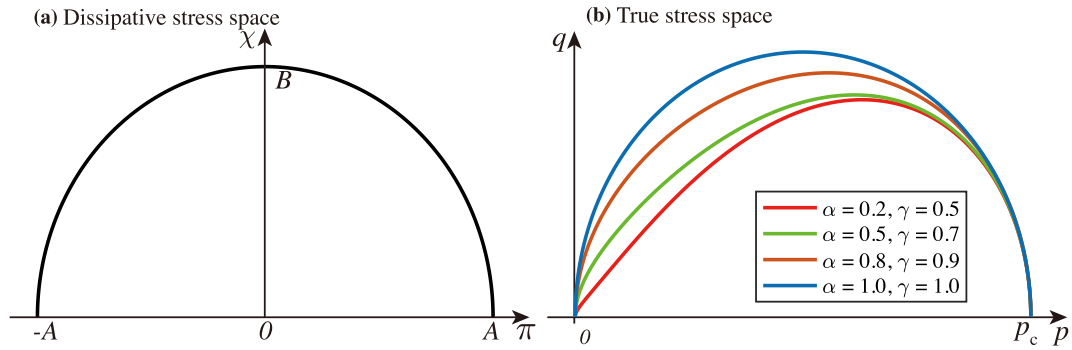

Figure 1. Yield function in (a) dissipative stress space and (b) true stress space. With the variation of α and γ as introduced in Equation 12, the ellipse yield locus in the dissipative stress space is distorted in the true stress space, where the consolidation pressure p_c defines a cap to the elastic domain.

For Equation 14 to hold, it requires that either (a) the dissipation function $\hat{\Phi}$ is zero, which means there is no plastic deformation and no energy is dissipated, that is, within the elastic regime, or (b) energy dissipation takes place and the plastic deformation is not null. For the latter case, the dissipative stress invariants should satisfy the following yield function

$$\mathcal{F} = \sqrt{\frac{\pi^2}{A^2} + \frac{\chi^2}{B^2}} - 1 = 0 \tag{15}$$

It can be found that Equation 14 is similar to the Kuhn-Tucker condition in the classical plasticity theory (Simo & Hughes, 2006), while the only difference is that Equation 14 is formulated in the dissipative stress space (π, χ), where the yield locus is an ellipse of semi-axes A and B (see Figure 1a) as described by Equation 15. Similarly, the classical return mapping strategy can be used here to determine the flow rules in the dissipative stress space via

$$\dot{\varepsilon}_v^p = \dot{\lambda}\frac{\partial \mathcal{F}}{\partial \pi}, \quad \dot{\gamma}^p = \dot{\lambda}\frac{\partial \mathcal{F}}{\partial \chi} \tag{16}$$

where $\dot{\lambda}$ is the rate form of the strain multiplier which satisfies $\mathcal{F} = 0$. Given that both the yield condition and flow rules are formulated in the (π, χ) space, the transition to the real stress space can be realized by considering the relationship in Equation 6b. To determine the shift stress, the following plastic free energy is adopted for the critical state line models (Collins, 2003)

$$\psi^p(\varepsilon^p) = \frac{1}{2}\Lambda\gamma p_c\left(\varepsilon_v^p\right) = \frac{1}{2}\Lambda\gamma p_c^0 \exp\left(\frac{\varepsilon_v^p}{\Lambda}\right) \tag{17}$$

where Λ is the material constant known as the plastic compressibility and p_c^0 the initial consolidation pressure. Thus, the shift pressure is evaluated as

$$\varrho = \frac{\partial \psi^p}{\partial \varepsilon_v^p} = \frac{1}{2}\gamma p_c^0 \exp\left(\frac{\varepsilon_v^p}{\Lambda}\right) \tag{18}$$

which gives rise to the (true) mean effective stress p and the deviatoric stress q

$$p = \varrho + \pi, \quad q = \chi \tag{19}$$

and the previous ellipse yield locus in the dissipative stress space is distorted in the true stress space as shown in Figure 1b. The merit of using the forementioned thermomechanics framework to derive constitutive laws is that it can allow non-associative flow rules in the true stress space whereas maintaining associative flow rules in the

dissipative stress space, and most importantly, the thermodancamic principles are preserved in the derivation procedure (Collins, 2003; Collins & Houlsby, 1997; Jacquey & Regenauer-Lieb, 2021).

2.1.2. Extension to Damageable Materials

As an extension of the above-described elasto-plastic model, a damage mechanics framework is incorporated into the constitutive formulation. The use of damage mechanics allows for the consideration of dynamic alteration of macroscopic properties, for example, the elastic moduli, without characterizing the microscopic geometry details but rather by introducing an entropy inspired damage intensity variable which is driven by the thermodynamics forces associated with the microscopic processes. Here, we consider a scalar damage intensity variable α_d to characterize the ratio of the effective area over the total area in a damageable material, and the elastic Helmholtz free energy for damageable materials now becomes

$$\Psi^e(\boldsymbol{\varepsilon},\alpha_d) = \frac{1}{2}K(1-\alpha_d)\left(\varepsilon_v^e\right)^2 + \frac{3}{2}(1-\alpha_d)\,G(\gamma^e)^2 \tag{20}$$

with $\alpha_d = 0$ corresponding to no damage while $\alpha_d = 1$ meaning the material is fully damaged. The generalized damage force dual to α_d can be expressed by the true stress invariants as

$$\tilde{\chi}_d = -\frac{\partial \Psi}{\partial \alpha_d} = \frac{1}{2(1-\alpha_d)^2}\left(\frac{p^2}{K} + \frac{q^2}{3G}\right) \tag{21}$$

Similar to Equation 11, the dissipation function which includes the damage effect can be formulated as follows

$$\hat{\Phi} = \sqrt{\left(\frac{A}{r_v}\dot{\varepsilon}_v^p\right)^2 + \left(\frac{B}{r_s}\dot{\gamma}^p\right)^2 + \left(\frac{C}{r_d}\dot{\alpha}_d\right)^2} \tag{22}$$

where r_s, r_v, r_d are coefficients associated with the contribution of shear, volumetric and damage deformation to the total dissipated energy and they satisfy the following relationship (Mir et al., 2018)

$$r_v^2 + r_s^2 + r_d^2 = 1 \tag{23}$$

Equation 22 is an extension of the original dissipation function (11) for critical state models, where three more coefficients r_v, r_s, r_d are introduced to control the dissipation characteristics of damageable elasto-plastic materials. It will be demonstrated in the following that these coefficients are able to affect the damage evolution, resulting in different types of localisation patterns in numerical simulations.

We note here that the bulk modulus and the shear modulus are linearly dependent on variable α_d representing the damage intensity, that is, the extent of microcracking in a representative elementary volume (REV) selected around a material point. As a REV-averaged quantity, a scalar representation is adopted for the damage intensity α_d corresponding to the degree of mechanical degradation in the material properties. The model hence implies applicability to two types of materials: (a) isotropic materials with mechanical properties reasonably assumed as isotropic during material degradation, and (b) materials that respond to mechanical loading with microcracks arising in plasticity zones in random directions. For materials under cyclic loading conditions where directional damage memory develops (Browning et al., 2018), an extension of the current model to a tensorial representation of damage will suit. Our primary aim of this contribution is to first develop a thermodynamically consistent model with a relatively simple mathematical form which can characterize different post-localisation features observed in limestone experiments. We seek a mathematical model capable of describing both the well-known discrete as well as the diffuse mode of compaction band successfully reproduced in the laboratory. We will demonstrate that our model as a self-consistent thermodynamic formulation underpins the selection mechanism favoring one post-localisation mode over the other under prescribed conditions.

Based on the above dissipation function, the dissipative stress invariants can be expressed as

$$\pi = \frac{\partial \hat{\Phi}}{\partial \dot{\varepsilon}_v^p} = \frac{A^2 \dot{\varepsilon}_v^p}{r_v^2 \hat{\Phi}} \tag{24}$$

$$\chi = \frac{\partial \hat{\Phi}}{\partial \dot{\gamma}^p} = \frac{B^2 \dot{\gamma}^p}{r_s^2 \hat{\Phi}} \tag{25}$$

$$\chi_d = \frac{\partial \hat{\Phi}}{\partial \dot{\alpha}_d} = \frac{C^2 \dot{\alpha}_d}{r_d^2 \hat{\Phi}} \tag{26}$$

where χ_d is the newly introduced dissipative damage force. Adopting the same procedure as that in Section 2.1.1, the yield function for the damageable materials now becomes

$$\mathcal{F} = \sqrt{r_v^2 \frac{\pi^2}{A^2} + r_s^2 \frac{\chi^2}{B^2} + r_d^2 \frac{\chi_d^2}{C^2}} - 1 = 0 \tag{27}$$

and the flow rules can be expressed as

$$\dot{\varepsilon}_v^p = \dot{\lambda} \frac{\partial \mathcal{F}}{\partial \pi} = \dot{\lambda} \frac{r_v^2}{(1+\mathcal{F})} \frac{\pi}{A^2} \tag{28}$$

$$\dot{\gamma}^p = \dot{\lambda} \frac{\partial \mathcal{F}}{\partial \chi} = \dot{\lambda} \frac{r_s^2}{(1+\mathcal{F})} \frac{\chi}{B^2} \tag{29}$$

$$\dot{\alpha}_d = \dot{\lambda} \frac{\partial \mathcal{F}}{\partial \chi_d} = \dot{\lambda} \frac{r_d^2}{(1+\mathcal{F})} \frac{\chi_d}{C^2} \tag{30}$$

Similar to Equation 12, quantities A, B and C can be related to the true pressure and damage variables as follows

$$A = \frac{(1-\gamma)}{(1-\alpha_d)} p + \frac{1}{2} \gamma p_c \tag{31}$$

$$B = \mu \left[p - \alpha \sqrt{1-\alpha_d} \left(p - \frac{1}{2} \gamma p_c \right) \right] \tag{32}$$

$$C = \frac{r_d \bar{\chi}_d}{\sqrt{\left(r_s^2 + r_d^2\right) \frac{\left(p - 0.5\gamma p_c\right)^2}{A^2} + \left(r_v^2 + r_d^2\right) \frac{q^2}{B^2}}} \tag{33}$$

Inserting Equations 31–33 into Equation 27, the same yield function as that used for elasto-plastic materials can be recovered

$$\mathcal{F} = \sqrt{\frac{\pi^2}{A^2} + \frac{\chi^2}{B^2}} - 1 = 0 \tag{34}$$

Likewise, by combining Equations 28–30, the damage evolution equation can be further described in terms of the volumetric and shear plastic strain rate as

$$\dot{\alpha}_d = \frac{\left(r_s^2 + r_d^2\right) \pi}{r_v^2 \bar{\chi}_d} \dot{\varepsilon}_v^p + \frac{\left(r_v^2 + r_d^2\right) \chi}{r_s^2 \bar{\chi}_d} \dot{\gamma}^p \tag{35}$$

2.2. Localisation Criterion Determined by Acoustic Tensor Approach

The classical bifurcation theory for strain localisation in elasto-plastic materials is based on a standing wavelength solution of acceleration waves (Rudnicki & Rice, 1975). The theory has formed the basis of many experimental and numerical experiments described by the following constitutive relationship:

$$\delta\sigma_{ij} = \mathbb{D}^{\mathrm{ep}}_{ijkl} : \delta\varepsilon_{kl} \tag{36}$$

where $\mathbb{D}^{\mathrm{ep}}_{ijkl}$ is the fourth-order elasto-plastic tensor relating a small increment of strain to a small increment of stress. The onset of bifurcation from a homogeneous state to localized deformation is attributed to the loss of positive definiteness of the acoustic tensor defined as

$$\Gamma_{ik} = n_j \mathbb{D}^{ep}_{ijkl} n_l \tag{37}$$

where $\boldsymbol{n}$ is the unit normal vector perpendicular to the localization plane.

We consider the tangent tensor for the damageable elasto-plastic materials and first formulate the increments of stress, plastic strain and damage respectively as.

$$\delta\sigma_{ij} = (1-\alpha_d)\,\mathbb{C}_{ijkl} : (\delta\varepsilon_{kl} - \delta\varepsilon^p_{kl}) - \frac{\sigma_{ij}}{1-\alpha_d}\delta\alpha_d \tag{38a}$$

$$\delta\varepsilon^p_{kl} = \delta\lambda^p \frac{\partial \mathcal{F}}{\partial \chi_{ij}} \tag{38b}$$

$$\delta\alpha_d = \delta\lambda^p \frac{\partial \mathcal{F}}{\partial \chi_d} \tag{38c}$$

Where $\delta\lambda^p$ is the plastic multiplier increment and $\mathcal{F}$ the yield condition. By substituting Equation 38 into the following consistency condition,

$$\delta\mathcal{F} = \frac{\partial \mathcal{F}}{\partial \sigma_{ij}} : \delta\sigma_{ij} + \frac{\partial \mathcal{F}}{\partial \varepsilon^p_{ij}} : \delta\varepsilon^p_{ij} + \frac{\partial \mathcal{F}}{\partial \alpha_d} : \delta\alpha_d \tag{39}$$

the plastic multiplier increment can be determined explicitly as

$$\delta\lambda^p = \frac{(1-\alpha_d)\frac{\partial \mathcal{F}}{\partial \sigma_{ij}} : \mathbb{C}_{ijkl} : \delta\varepsilon_{kl}}{\frac{\partial \mathcal{F}}{\partial \sigma_{ij}} : \left((1-\alpha_d)\,\mathbb{C}_{ijpq} : \frac{\partial \mathcal{F}}{\partial \chi_{pq}} + \frac{\sigma_{ij}}{1-\alpha_d}\frac{\partial \mathcal{F}}{\partial \chi_d}\right) - \frac{\partial \mathcal{F}}{\partial \varepsilon^p_{ij}} : \frac{\partial \mathcal{F}}{\partial \chi_{ij}} - \frac{\partial \mathcal{F}}{\partial \alpha_d}\frac{\partial \mathcal{F}}{\partial \chi_d}} = P_{kl} : \delta\varepsilon_{kl} \tag{40}$$

Combining Equation 40 and Equation 38, the tangent damage elasto-plastic tensor reads

$$\mathbb{D}^{ep}_{ijkl} = (1-\alpha_d)\,\mathbb{C}_{ijkl} - (1-\alpha_d)\,\mathbb{C}_{ijpq} : \frac{\partial \mathcal{F}}{\partial \chi_{pq}} P_{kl} - \frac{\sigma_{ij}}{1-\alpha_d} P_{kl} \frac{\partial \mathcal{F}}{\partial \chi_d} \tag{41}$$

With this tangent tensor, the localization criterion can be assessed by calculating the determinant of acoustic tensor as defined in Equation 37.

$$\det(\boldsymbol{\Gamma}) \leq 0 \tag{42}$$

For a triaxial geometry as illustrated in Figure 2a, the unit vector $\boldsymbol{n}$ for characterizing the localization plane can be determined by two angles θ and φ, giving rise to the following expression of $\boldsymbol{n}$

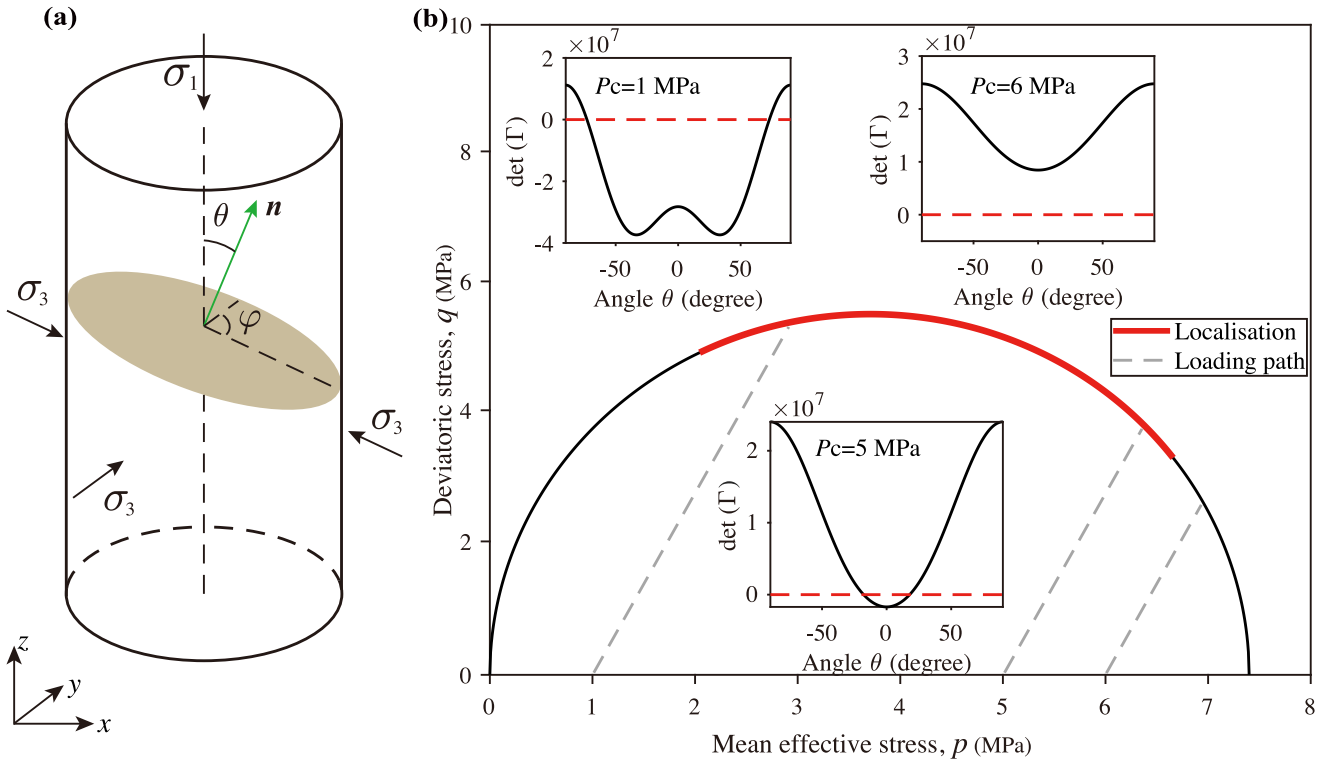

Figure 2. (a) Illustration of the localisation plane emerging in a triaxially compressed cylindrical rock specimen. The normal $\boldsymbol{n}$ to the localized plane can be determined by the angle θ and φ. (b) Localisation domain for the Modified Cam-Clay model in the true stress space. The insets demonstrate the localisation criterion as a function of the plane angle θ under various confining pressure.

$$\boldsymbol{n} = \begin{pmatrix} \sin(\theta)\sin(\varphi) \\ \sin(\theta)\cos(\varphi) \\ \cos(\theta) \end{pmatrix} \tag{43}$$

to simplify the analysis we consider the value of φ is fixed at $\pi/2$ and the localisation plane is now only determined by θ which defines the angle between the localisation plane and the axial loading direction. Figure 2b shows the determinant of acoustic tensor for the damageable elasto-plastic material at a given set of parameters as listed in Table 1. It can be found that the occurrence of localized deformation is dependent on confining pressure P_c. When P_c is small, the determinant of acoustic tensor takes its minimum value at large θ, corresponding to the formation of high-angle shear bands. While as confining pressure increases to certain large level, for example, 5 MPa, the localisation plane can become perpendicular to the axial loading direction with $\theta = 0$.

Table 1
Calibrated Parameters From the Triaxial Experiments

Parameter	Symbol	Value	Units
Young's modulus	E	525	MPa
Poisson's ratio	ν	0.17	-
Friction coefficient	μ	1.5	-
Plastic compressibilities	Λ	2	-
Consolidation pressure	p_c	7.4	MPa
Yielding shape coefficient	α	0.91	-
	γ	0.91	-
Dissipation splitting coefficient	r_v	0.76	-
	r_d	0.5	-

The above analysis is a widely used methodology for determining the localisation onset of a rate-independent Cauchy medium. For more sophisticated models, including the rate-dependent Cauchy continuum (Stathas & Stefanou, 2022), Cosserat or higher order continua (Abdallah et al., 2020; Rattez et al., 2018) and multiphysics coupling processes (Hu et al., 2017; Jacquey, Rattez, & Veveakis, 2021), the more general eigenvalue analysis is needed. With the combination of perturbation method, the acoustic tensor approach can be extended to take the form of a classical eigenvalue problem, where the bifurcation behaviors rely on the eigenvalues of the acoustic tensor as well as the perturbation wavelength (Stefanou & Gerolymatou, 2019). More detailed descriptions about the bifurcation analysis are out of the scope of this contribution, and we guide the readers to the above mentioned literature.

1. Known database at time step t_{n} : $\varepsilon^{\mathrm{p}}_{v,n}, \boldsymbol{\sigma}_{\mathrm{n}}, \alpha_{d,\mathrm{n}}$
2. Given strain increment at time step $t_{\mathrm{n+1}}$: $\Delta\boldsymbol{\varepsilon}_{\mathrm{n+1}}$
3. Computer elastic trial stress:
   $\boldsymbol{\sigma}^{\mathrm{tr}}_{\mathrm{n+1}} = \boldsymbol{\sigma}_{\mathrm{n}} + (1-\alpha_{d,\mathrm{n}})\mathbb{C} : \Delta\boldsymbol{\varepsilon}_{\mathrm{n+1}}, \quad p^{\mathrm{tr}}_{\mathrm{n+1}} = -\frac{\mathrm{trace}(\boldsymbol{\sigma}^{\mathrm{tr}}_{\mathrm{n+1}})}{3}, \quad \boldsymbol{s}^{\mathrm{tr}}_{\mathrm{n+1}} = \boldsymbol{\sigma}^{\mathrm{tr}}_{\mathrm{n+1}} + p^{\mathrm{tr}}_{\mathrm{n+1}}\boldsymbol{I}, \quad q^{\mathrm{tr}}_{\mathrm{n+1}} = \sqrt{\frac{3}{2}}\|\boldsymbol{s}^{\mathrm{tr}}_{\mathrm{n+1}}\|, \quad \boldsymbol{n} = \frac{\boldsymbol{s}^{\mathrm{tr}}_{\mathrm{n+1}}}{\|\boldsymbol{s}^{\mathrm{tr}}_{\mathrm{n+1}}\|}, \quad \varrho^{\mathrm{tr}}_{\mathrm{n+1}} = 0.5\gamma p^{0}_{\mathrm{c}} \exp(\frac{1}{\Lambda} \times \varepsilon^{p}_{v,n}),$
   $\pi^{\mathrm{tr}}_{\mathrm{n+1}} = p^{\mathrm{tr}}_{\mathrm{n+1}} - \varrho^{\mathrm{tr}}_{\mathrm{n+1}}, \quad \chi^{\mathrm{tr}}_{\mathrm{n+1}} = q^{\mathrm{tr}}_{\mathrm{n+1}}$
4. Check $\mathcal{F} = \sqrt{\frac{\pi^{\mathrm{tr2}}_{\mathrm{n+1}}}{A^{2}_{\mathrm{n+1}}} + \frac{\chi^{\mathrm{tr2}}_{\mathrm{n+1}}}{B^{2}_{\mathrm{n+1}}}} - 1 > \mathrm{tol}$?
   No, elastic step, set $\boldsymbol{\sigma}_{\mathrm{n+1}} = \boldsymbol{\sigma}^{\mathrm{tr}}_{\mathrm{n+1}}$, $\varepsilon^{p}_{v,\mathrm{n+1}} = \varepsilon^{p}_{v,\mathrm{n}}$ and exit
5. Yes, plastic step, solve for $\Delta\varepsilon^{p}_{v}, \Delta\gamma^{p}$ such that $\mathcal{F} = \sqrt{\frac{\pi^{2}_{\mathrm{n+1}}}{A^{2}_{\mathrm{n+1}}} + \frac{\chi^{2}_{\mathrm{n+1}}}{B^{2}_{\mathrm{n+1}}}} - 1 < \mathrm{tol}$
6. Computer final stress and exit:
   $\varepsilon^{\mathrm{p}}_{v,\mathrm{n+1}} = \varepsilon^{\mathrm{p}}_{v,\mathrm{n}} + \Delta\varepsilon^{\mathrm{p}}_{v}, \quad p_{\mathrm{n+1}} = p^{\mathrm{tr}}_{\mathrm{n+1}} - (1-\alpha_{d,\mathrm{n+1}})K\Delta\varepsilon^{\mathrm{p}}_{v},$
   $q_{\mathrm{n+1}} = \chi_{\mathrm{n+1}} = q^{\mathrm{tr}}_{\mathrm{n+1}} - 3(1-\alpha_{d,\mathrm{n+1}})G\Delta\gamma^{\mathrm{p}}, \quad \varrho_{\mathrm{n+1}} = \varrho^{\mathrm{tr}}_{\mathrm{n+1}} \exp(\frac{1}{\Lambda} \times \Delta\varepsilon^{p}_{v}),$
   $\pi_{\mathrm{n+1}} = p_{\mathrm{n+1}} - \varrho_{\mathrm{n+1}}, \quad \boldsymbol{\sigma}_{\mathrm{n+1}} = -p_{\mathrm{n+1}}\boldsymbol{I} + \sqrt{\frac{2}{3}}q_{\mathrm{n+1}}\boldsymbol{n}$
   ($\boldsymbol{I}$ is the second-rank identity tensor)

Figure 3. Stress update procedure for the Modified Cam-Clay model.

2.3. Reaction-Diffusion Approach to Regularize the Localisation Pattern

In the above elasto-plastic-damageable formulations, there is no explicit consideration of the localized pattern's length scale. To remedy this, we consider the localized band as a diffusive damage zone governed by a length scale parameter l, and the development of this damage zone has a characteristic diffusion velocity $\mathcal{G}_c$ (a characteristic entropic velocity of the reaction-diffusion process, see Regenauer-Lieb and Hu (2023) for a derivation), which recasts the damage evolution equation into

$$\dot{\alpha}_d = \mathcal{G}_c\left(l\nabla^2\alpha_d - \frac{\alpha_d}{l}\right) + \frac{\left(r_s^2 + r_d^2\right)\pi}{r_v^2\bar{\chi}_d}\dot{\varepsilon}^{p}_{v} + \frac{\left(r_v^2 + r_d^2\right)\chi}{r_s^2\bar{\chi}_d}\dot{\gamma}^{p} \tag{44}$$

where the linear term with negative sign in the first bracket represents resistance to the diffusive spread of the damage zone evolution process. From a thermodynamic perspective this resistance term links to the postulate that the coupled positive-negative entropy production processes in the damage zone request an uphill diffusion process for mass balance (Regenauer-Lieb & Hu, 2023). The physical interpretation of this positive-negative couple is the evolution process of a compaction band caused by grain crushing in a porous medium. There, the outwards-diffusing low density phase of the crushed grains (or powder) represents the positive diffusion direction, whereas the inwards-diffusing densification of the matrix is identified as the negative (resisting) diffusion term. Both negative and positive diffusion processes need to equilibrate over the process time such that the width of the compaction band is established. The addition to the reaction-diffusion-type equation is completed by the last two positive reaction source terms on the RHS of Equation 44 related to plastic loading which promotes damage evolution. The approach presented here is motivated by a unification (Regenauer-Lieb & Hu, 2023) of approaches of the reaction-diffusion type; see for example, Veveakis and Regenauer-Lieb (2015) and Alevizos et al. (2017), where the concept of time-dependent processes was utilized to regularize sharp fracture topology into diffusive fracture zones without singularities in low permeable rocks. The existence of an entropic density l corresponds to an equilibrium state toward which the compaction band forming evolves.

2.4. Numerical Implementation

The above-described constitutive model along with the stress equilibrium and damage evolution equations are implemented in a finite element solver LEMUR (muLtiphysics of gEomaterials using MUltiscale Rheologies). The LEMUR simulator relies on the open-source MOOSE platform which is built upon state-of-the-art libraries including libMesh and PETSc (Cacace & Jacquey, 2017; Permann et al., 2020; Poulet et al., 2017; Tang &

Hu, 2023). It provides a flexible framework to solve multiphysics and multicomponent coupled problems implicitly with automatic differentiation and parallel computing.

The weak form of the governing equations can be found in the appendix while the stress update procedure for the Modified Cam-Clay (MCC) model is summarized in Figure 3, where a predictor-corrector scheme is utilized in our implementation. We first compute the trial stress based on the given strain increment at the current loading step. Then, the yield function will be checked in the dissipative trial stress space. If the value of this yield function in the dissipative stress space is smaller than the tolerance, this step will belong to an elastic step and the trial stress will be set as the final stress without correction. But if the yield function exceeds the tolerance, this step will be regarded as a plastic step and Newton-Raphson iterations (Jacquey, Regenauer-Lieb, & Cacace, 2021) will be needed to determine the plastic increment of the strain invariant $\varepsilon_v := -\varepsilon_{kk}$ and $\gamma := \sqrt{2/3}\|\boldsymbol{e}\|$, after which these two plastic components will be used to correct the trial stress and finalize the stress update. In the LEMUR simulator, the stress update procedure is implemented in a material module via the MOOSE framework while the stress equilibrium and damage evolution equations are implemented in kernel modules. MOOSE allows a tight coupling between these modules so that the variables (e.g., strain and damage) in kernels can be coupled into the material module to produce material properties (e.g., true and dissipative stresses), and in turn these properties can also be consumed by kernels so as to solve governing equations. An illustration of the coupling between different modules can be found in Appendix A1.

3. Results

3.1. Standard Thermomechanics Approach

To validate the model, we utilize the experimental results obtained from the highly porous Mt. Gambier limestone specimens tested in triaxial compression (Chen et al., 2020a, 2020b, 2022). The laboratory tests were conducted based on two groups of specimens. One group has relatively large size, with the diameter of 30 mm and the height of 60 mm, which is used for the mechanical tests, whereas another group has relatively small size ($h = 25.4$ mm $d = 12.7$ mm), which is prepared for observing the compaction band formation using microCT. We adopted a similar strategy for our numerical simulations, that is, the setup with the same geometric configuration as the former group is first utilized for benchmarking the mechanical properties for example, strength and failure mode, after which we used a decreased geometry size (the same as the size of the latter group) for compaction banding investigation. The simulations consist of a pre-compressing of the specimen to certain hydrostatic pressure levels, and a following increase of the differential stress, simulating the loading sequence in the experiments.

Figure 4 displays the simulation results against the experimental data. It shows that the MCC model can well capture the mechanical data, with the deviatoric stress strength increasing first and then capped at higher mean effective stress. When confining pressure is at low level, the mechanical behaviors fall into the brittle faulting regime (Wong & Baud, 2012), where the formation of shear band appears to be the main failure mode. As confining pressure increases, the mechanical response of the sample may enter a transition zone before entering the final cataclastic flow region (Holcomb et al., 2007; Huang et al., 2019). Within the transition regime, the shear band would evolve into shear-enhanced compaction band or pure compaction band with an increased confining pressure. Three subfigures in Figure 4 notably indicate this progressive evolution of the failure pattern when the confining pressure is increased from 1 to 5 MPa, and the simulated failure modes are in good agreement with the experimental observations. The best fit parameters for the yield strength are listed in Table 1.

In addition to the strength and failure mode analysis, some representative deviatoric stress strain curves are presented in Figure 5. It is worthwile noting that by choosing an extreme end-member material (Mt. Gambier limestone which has a high porosity (50%)) we aim to test the model in the post-localisation characteristics at large compaction strain where mode changes (discrete vs. diffuse) have been observed in experiments. The advantage of the approach is that it allows investigation of the response for modes of compaction triggered by possible non-local gradients of the damage evolution in the post-localisation regime. One limitation of the current model is that the highly porous limestone is not ideally homogeneous and the effect of collapse of large pores may lead to noisy data on lateral strain. The effect of the collapse of large pores is especially noticeable at the beginning of the experiment where the model prediction for an ideal homogeneous material may not well match the observed axial strain of the heterogeneous sample, albeit the assumption of the sample undergoing an isotropic

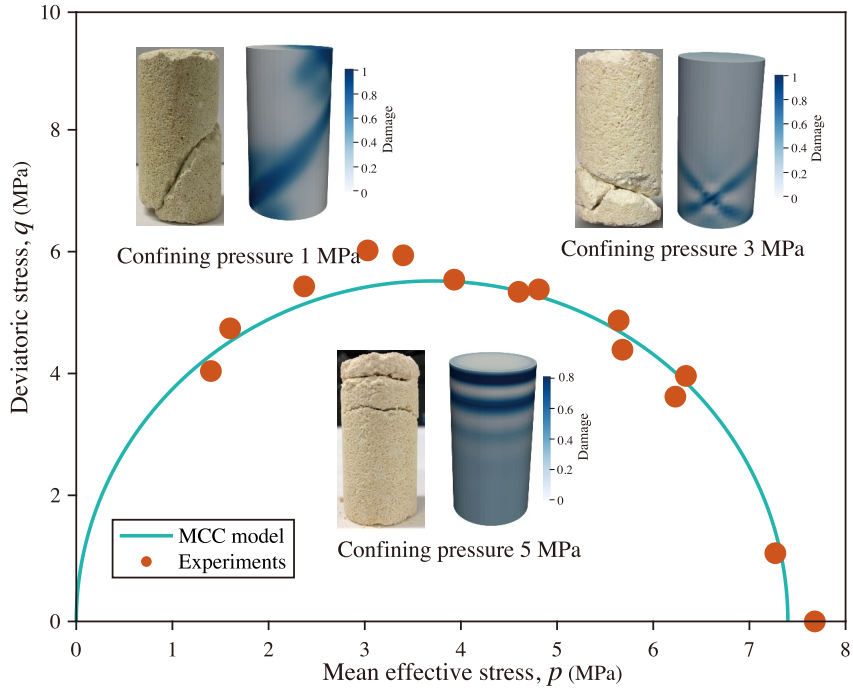

Figure 4. Initial yield stress and failure mode of Mt. Gambier limestone samples obtained from laboratory triaxial tests (Chen et al., 2020a, 2020b, 2022) and the Modified Cam-Clay model.

degradation at the upscaled level may still reasonably hold. The simulation therefore aims to match the data when a consistent strain hardening shows up at the post-yielding regime after a system-spanning localisation appears (the prominent rapid softening shown in experimental data), accompanied with periodic stress drops. This is observed when the compaction strain is large and the confining pressure is high (Figure 5b). The stress drops at the high confining pressure scenario may be related to the mechanism of pore collapse and grain crushing (Abdallah et al., 2020, 2021), which tends to tighten the packing of microscopic configurations and thus results in stress redistribution across the specimen (Fossen et al., 2018; Sulem & Vardoulakis, 1995). This point is

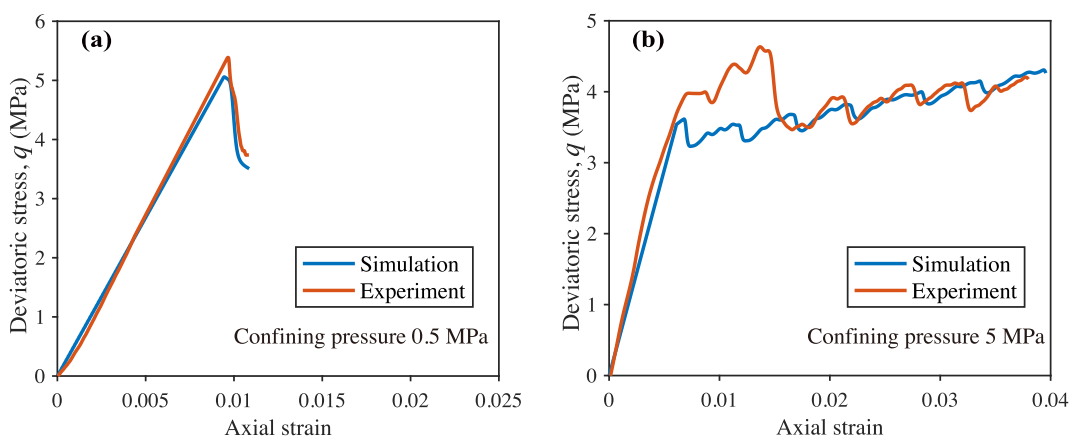

Figure 5. Representative deviatoric stress strain response at different confining pressures: (a) Strain softening occurs after yielding at 0.5 MPa confining pressure. (b) Strain hardening shows up at the post-yielding regime, accompanied with recurring stress drops when confining pressure is 5 MPa. We attribute the initial stages of the experiment to the effect of collapse of large pores, reflecting the initial heterogeneity of the porous limestone as documented by CT-scans (Chen et al., 2020a). The sample shows a consistent overall hardening trend after the internal heterogeneities have collapsed at an axial strain of around 0.015. Simulation parameters were selected based on matching the post-yielding regime data where a consistent strain hardening appears with periodic stress drops.

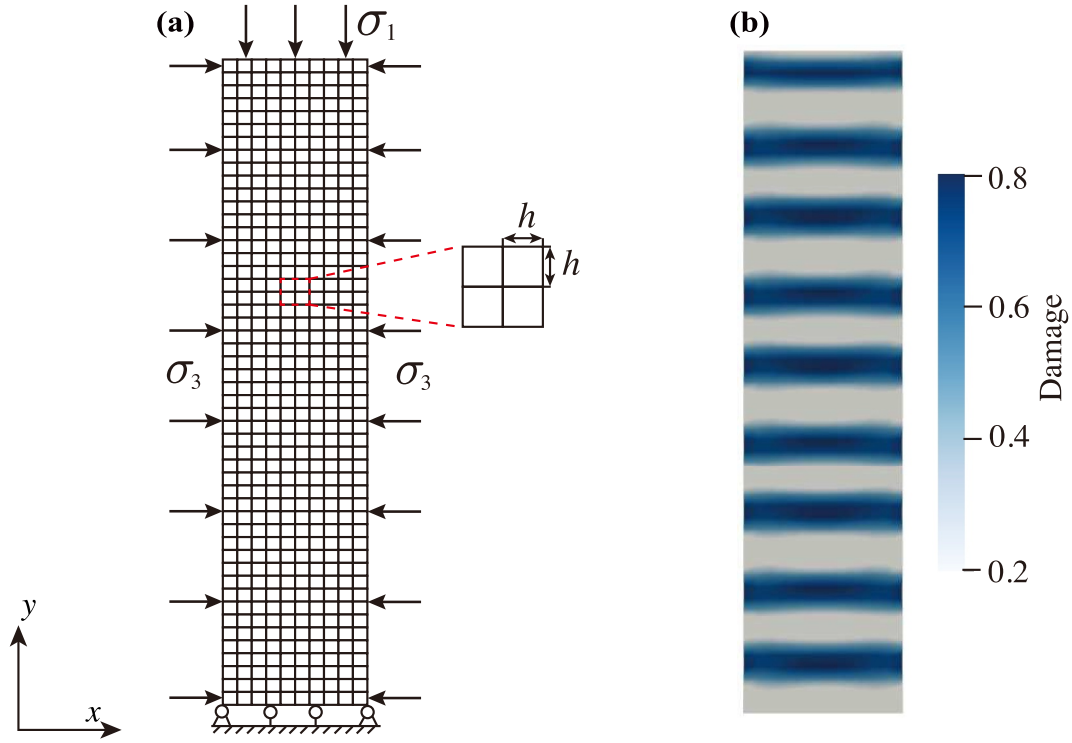

Figure 6. Plane strain compression of limestone specimen: (a) Schematic of the numerical setup, where structured quadrilateral meshes with size h are used to discretize the space domain. The height of the setup is 25.4 mm and the aspect ratio height over width is 5. (b) Overview of the interlayered compaction band pattern illustrated by the distribution of damage intensity variable.

supported by the evidence presented in Section 3.3, where the porosity reduction is recorded via the X-ray CT analysis of compaction experiments.

The above benchmark analysis indicates that the MCC model formulated in the thermomechanics framework can characterize the mechanical response of highly porous limestones at different stress states. In what follows, we focus on the compactive failure regime underpinning the evolution of compaction band. Here the height of the numerical setup is reduced to 25.4 mm (see Figure 6a) in order to be consistent with the experiments. Meanwhile, for the purpose of computational efficiency, the 2D plane strain conditions were adopted for the simulation with the aspect ratio of specimens set as 5.0. The effect of the aspect ratio on the compaction band pattern will be presented in the next section. Figure 6b shows simulation results of a series of compaction bands appearing at a confinement of 5 MPa. Within the specimen, the array of discrete bands is equally spaced with the same thickness,

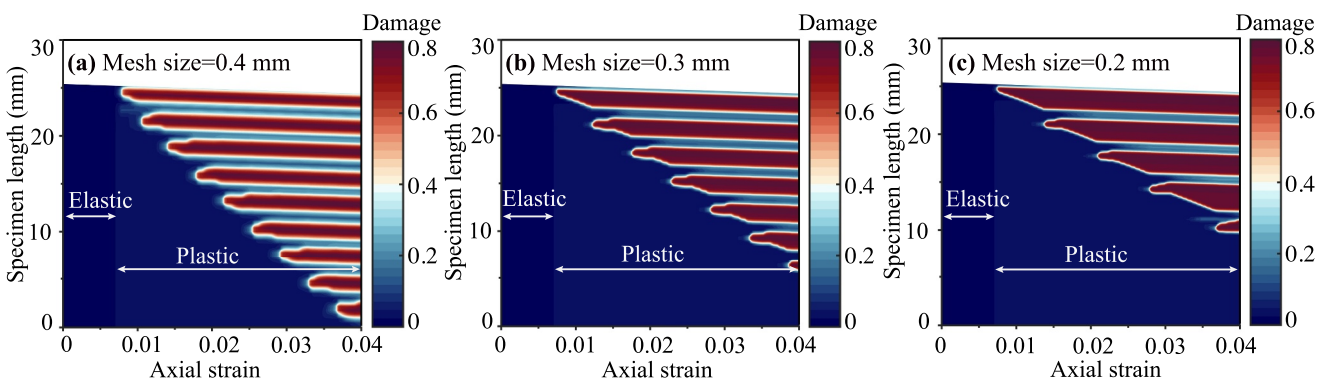

Figure 7. Sequential compaction band evolution and mesh dependency.

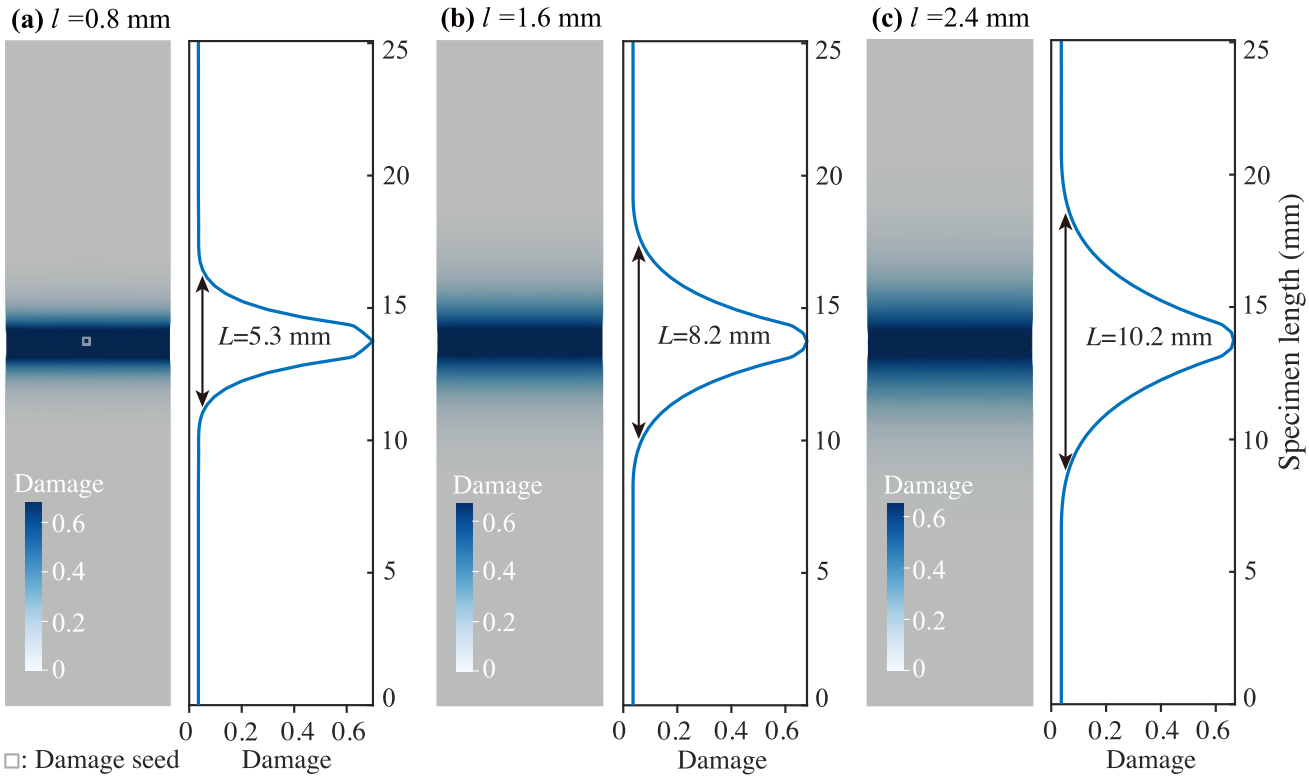

Figure 8. Effect of l on material imperfection induced compaction bands. The parameters used are $\mathcal{G}_c = 8 \times 10^{-7}$m/s, $r_d = 0.58$.

and the corresponding dynamic evolution of the compaction bands is presented in Figure 7. It demonstrates that the first band is triggered from the top boundary after the specimen undergoes a transition from the elastic to the plastic regime. After initiation, the first compaction band stays unchanged over time (as standing waves) and the next band will start to develop. This process will repeat until the specimen is saturated with the array of compaction bands. The material properties here are assumed as homogeneous in the numerical demonstration, while the effect of heterogeneity will be discussed in the Discussion. Quadrilateral elements were used in the numerical experiment with varying mesh size and mesh dependence reveals in the post-yield results. This is due to the lack of consideration about the internal length scale characterizing the dynamic process of band formation.

3.2. Extending the Thermomechanics Approach via Reaction-Diffusion Ansatz

Due to the inherent lack of internal length scale in the Thermomechanics Approach, mesh dependency inevitably shows up in the numerical simulation of the localisation patterns. In this section we extend the model through an entropic consideration of the reaction-diffusion type in the sense of introducing a characteristic diffusion rate as outlined in Section 2.3. The damage evolution Equation 35 used in Section 3.1 is hence now replaced by Equation 44, while all the other formulations and parameters remain the same.

With this entropy inspired regularization technique implemented in the model, the localisation band formation owns a diffusive nature controlled by a characteristic length scale l (see Equation 44). It is hence natural to study first the influence of this parameter of length on the forming of localisation patterns. Different from the sequential formation of compaction bands which are initially triggered by the top loading boundary in Figure 7, an initial damage seed with the value 0.01 (see the tiny square in Figure 8a) is imposed in the middle of the specimen in order to trigger the compaction banding. The simulation results in Figure 8 showcase that a compaction band is formed from the location where the initial material defect is assumed, with varying the value of l. When l is small, the damage band profile is relatively more localized with a smaller thickness, while as l increases a growth in the band width is observed with a more diffused profile, as shown in Figure 8. With the value of l increases from $l = 0.8$ mm to $l = 2.4$ mm, the width of the compaction band increases from 5.3 to 10.2 mm. Given that the band

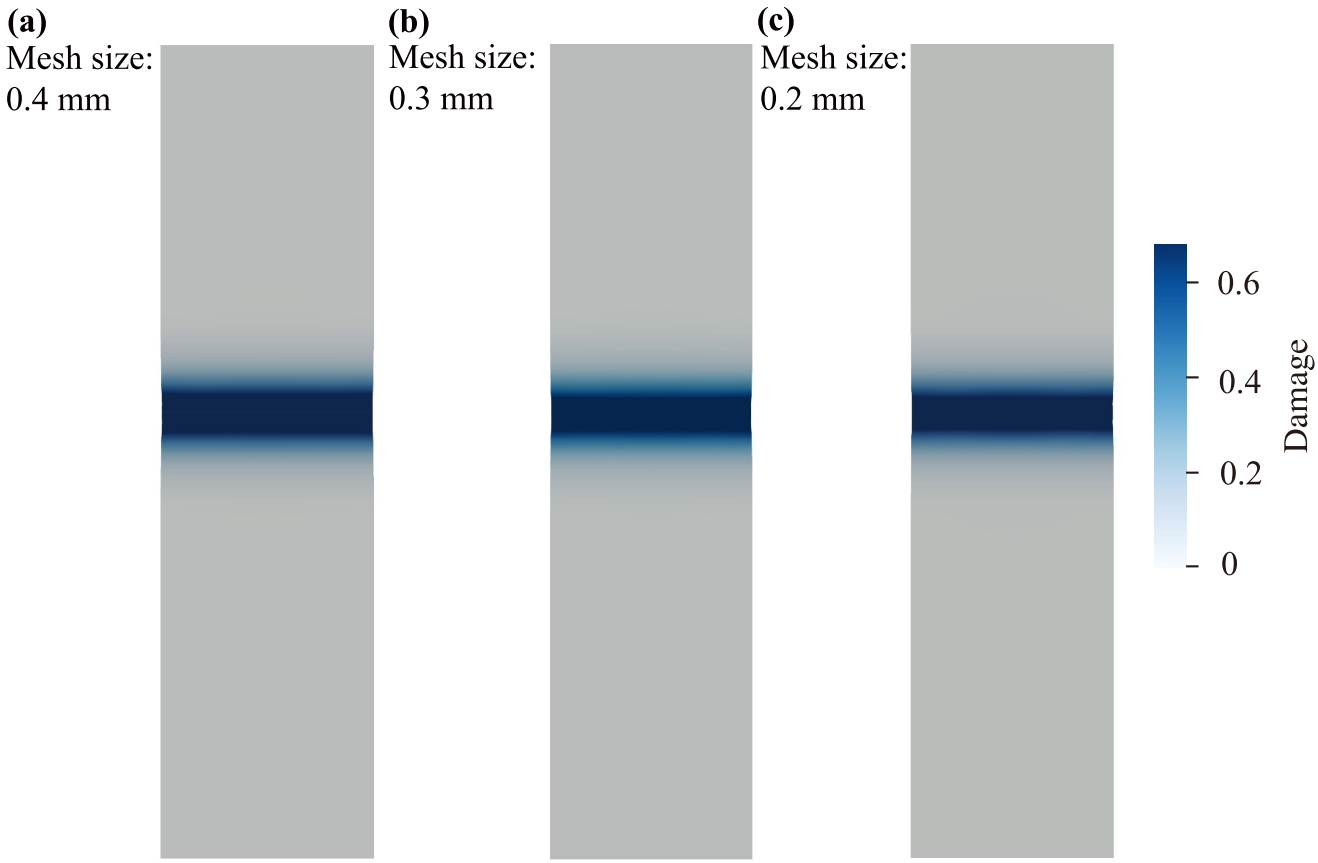

Figure 9. Compaction bands formed at different mesh sizes incorporating the reaction-diffusion regularization.

formation in Figure 7 without regularization is highly mesh-dependent due to missing of an internal length scale, we proceed to investigate how well the band width is regularized incorporating the length parameter l into the model by using different mesh sizes. The results in Figure 9 demonstrate that no significant variation is seen in the localization band width when the mesh size reduces by half from 0.4 to 0.2 mm at a given value of $l = 0.8$ mm. This suggests that the entropy inspired regularization technique that we propose in this study is capable of mitigating the mesh dependency problem by correcting the mathematical ill-posedness in the classical theories.

In addition to the length scale, a characteristic velocity parameter $\mathcal{G}_c$ is also introduced in the damage evolution equation. This parameter has recently been introduced to complete the reaction-diffusion framework proposed in (Alevizos et al., 2017) through an entropic velocity (Regenauer-Lieb & Hu, 2023) derived from upscaling the entropy production of multiple coupled micro-slip phenomena. Since this parameter is related to the diffusive effect during the localized pattern formation, it can be inferred that if $\mathcal{G}_c$ is assigned with a very large value, the generated damage zone may smear out the localized band ending up with appearing as a homogeneous pattern. Thus, the value of $\mathcal{G}_c$ is chosen relatively small and this inference can be supported by the quasi-static triaxial experiments on Diemelstadt sandstone (Townend et al., 2008), where the propagating velocity of the compaction band is found to be around 8×10^{-5} m/s. The value of $\mathcal{G}_c$ may vary depending on the material properties as well as the loading conditions.

In what follows, the effect of the magnitude of $\mathcal{G}_c$ on the localisation pattern formation will be demonstrated while the inversion of its value from lab experiments is deferred to the next section. Figure 10 depicts the band formation process with $\mathcal{G}_c$ ranging from $1 \times 10^{-8} \sim 8 \times 10^{-7}$ m/s. It shows that the compaction band initiates and develops from top to bottom in a sequential manner when there is no pre-existing damage, that is, no material imperfection seeding in the specimen. For a small value of $\mathcal{G}_c$, the axial strain needs to reach about 4% for the whole specimen to be saturated with an array of bands. For a larger value $\mathcal{G}_c$, the compaction band array occupies the whole specimen at a smaller axial strain. This suggests that a larger $\mathcal{G}_c$ accelerates the formation of compaction

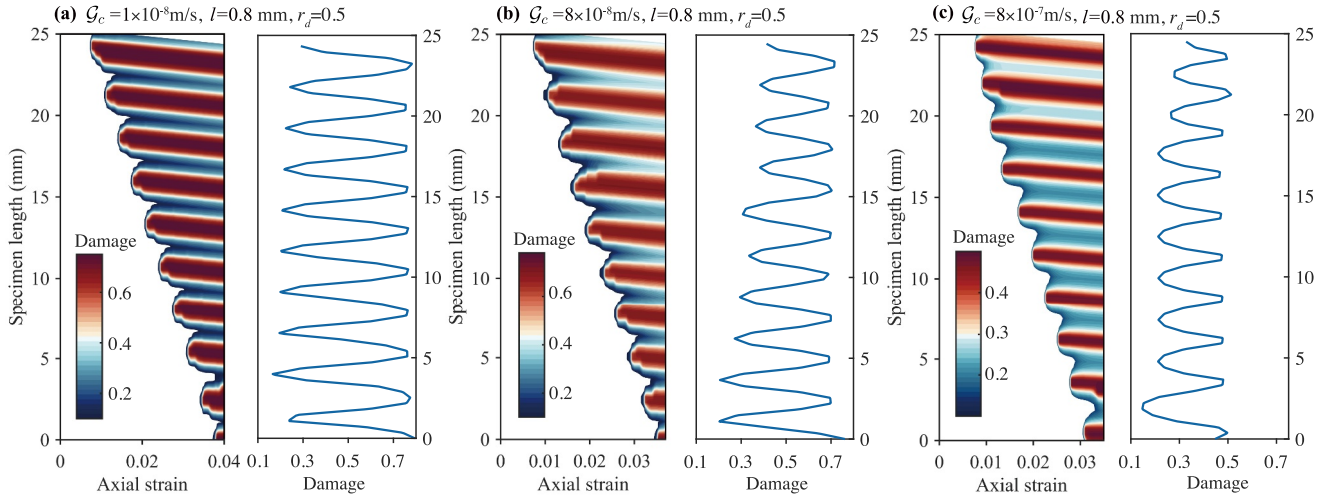

Figure 10. Effect of $\mathcal{G}_c$ on the evolution of compaction band arrays.

bands whereas a smaller $\mathcal{G}_c$ prolongs the banding formation process. Besides, the variation of $\mathcal{G}_c$ also affects the damage distribution along the specimen as well as the maximum value of damage within the localized bands as demonstrated in Figure 10, which is about 0.8 for $\mathcal{G}_c = 1 \times 10^{-8}$ (Figure 10a) and decreasing to around 0.5 for $\mathcal{G}_c = 1 \times 10^{-8}$ (Figure 10c).

The above analysis focuses on the parameter study of the newly introduced diffusion term in Equation 44. In what follows, the effect of the last two reaction terms on the localisation pattern formation and the interactions between the reaction terms and the diffusion term will be explored. For this purpose, different values of the dissipation splitting coefficient r_d and $\mathcal{G}_c$ are utilized for investigating the damage source terms and the diffusion term, respectively. The corresponding localisation pattern is then analyzed by the total number of damage bands, the average band thickness and the distance between each band, at a fixed axial strain of 3.5%. The results are summarized into heat-maps shown in Figure 11a. It shows that fewer bands appear when r_d is relatively large and this is especially the case when the parameter $\mathcal{G}_c$ is also small. Notably, for cases falling into the bottom-right region in Figure 11a1, there is only one band formed, and this single band keeps growing its width after initiation during the whole loading process, resulting in the largest valus of the mean band thickness, that is, the bottom-right corner of Figure 11a2. By contrast, when r_d is relatively small or when $\mathcal{G}_c$ is large, a larger number of bands form along the specimen and the formation process is akin to the standing wave solution with regular band thickness and spacing. Based on the distinct differences in pattern formation, the parametric space is divided into three zones separated by the red line as shown in Figure 11, which can be interpreted as a result of the interplay between the reaction source terms and the diffusion term. Within Zone 1 (see the labeling in Figure 11), the last two damage source terms in Equation 44 become dominant due to relatively large r_d, and the diffusion is relatively insignificant in this case. Consequently, the damage source arising from the plastic deformation can not diffuse efficiently to trigger the compaction band arrays, but rather nucleate and coalesce in one single band with an increase in the band thickness under loading. In Zone 2, the diffusive effect becomes significant because of large $\mathcal{G}_c$, so that the damage source can diffuse effectively to trigger new compaction bands during the process. For Zone 3, more than one discrete band appears in the specimen while the source terms may still cause some damage coalescence, and hence the pattern morphology is classified as an in-between region.

The aspect ratio of the specimen in the above analysis is fixed as height over width $H/W = 5$ (see Figure 6a). In what follows, we investigate the morphology of localisation patterns at different aspect ratios by fixing the height as 25.4 mm and altering the width. The combined effect of aspect ration and the dissipation splitting coefficient r_d on the damage band characteristics is summarized in Figure 11b, in which the heat-maps are also divided into 3 zones, according to the number of bands generated in the specimen, similar as in Figure 11a. The value of the mean band thickness and that of the mean distance between bands in millimeter are shown in Figures 11b2 and 11b3, respectively. Note that with the aspect ratio decreasing from 5 to 2, the average thickness of the band array increases, for example, from about 2.6 to 6.8 mm at $r_d = 50\%$. This implies that under the proposed reaction-

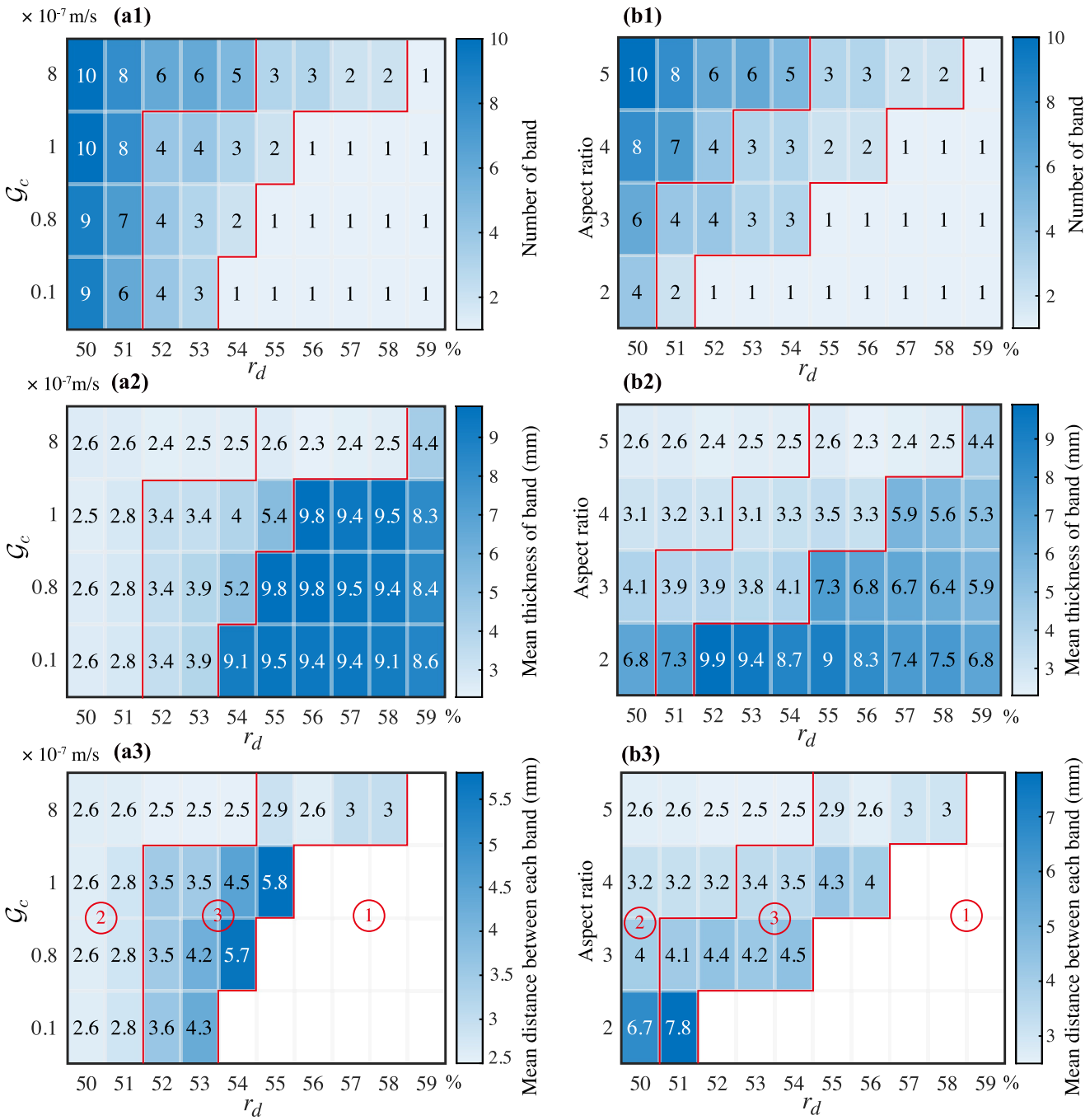

Figure 11. Parametric diagram for the formation of compaction bands. The left panel (a1–a3) manifests the effect of $\mathcal{G}_c$ and r_d on the pattern formation at a fixed aspect ratio. The parametric space is categorized into 3 zones as separated by the red line. For Zone 1 with relatively large r_d, the damage source terms cannot diffuse efficiently to trigger compaction band arrays but rather nucleate and coalesce in one single band. While as $\mathcal{G}_c$ becomes relatively large in Zone 2 or Zone 3, the damage source can diffuse effectively to trigger new compaction bands. The right panel (b1–b3) shows the combined influence of the aspect ratio and r_d at a fixed value of $\mathcal{G}_c$, also divided into 3 zones. The variation of the band width implies that the length characteristic of the compaction band is not an intrinsic material property but dependent also on the specimen geometry and loading conditions.

diffusion regularization, the band thickness is not intrinsic (i.e., solely determined by the material properties) but co-determined by the specimen geometry and loading conditions. In other words, the internal length scale here results from a dynamic interaction between the local and global scales that governs the pattern formation process.

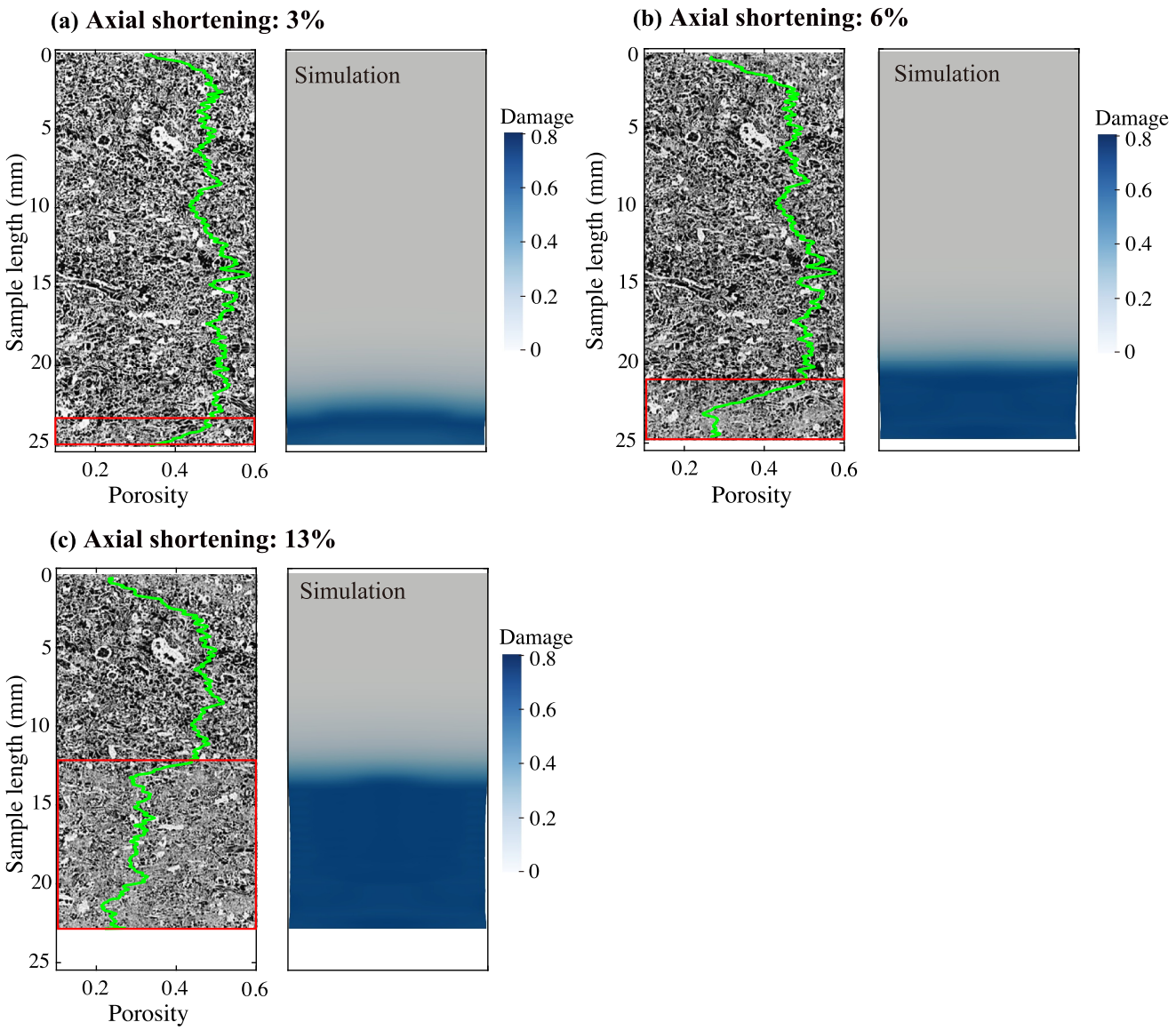

Figure 12. Comparison between the simulated diffuse compaction band and the porosity reduction profile obtained from the X-ray CT analysis at different loading stages in Mt. Gambier Limestone samples.

3.3. Comparison With Compaction Experiments on Mt. Gambier Limestone

In this section, the regularized numerical simulation results are compared with the compression experiments on Mt. Gambier Limestone. The experiments are conducted via an X-ray transparent triaxial cell with confining pressure set at 5 MPa. During the loading process, the X-ray CT scan is performed on the limestone sample at different strain levels so as to identify the micro-scale process associated with the compaction band formation.

The gray-scale map in Figure 12 is 2D slices of X-ray tomographs at three representative strain levels, where white color represents grains while black color represents pores. By virtue of the X-ray CT analysis, the porosity profile at each loading stage is also plotted in Figure 12 as depicted by the green line. It can be found that the compaction band initiates at the end of the sample with distinct porosity reduction, followed by progressive band growth in the axial compression direction. This type of compaction band can be identified as a diffuse band due to its width increasing characteristic. Given that the pattern formation within Zone 1 in Figure 11 also has such thickness coarsening behavior, the parameters within this zone can be candidates to generate analogous patterns numerically. Among these parametric candidates, as the use of different combinations of $\mathcal{G}_c$ and r_d leads to

Table 2
Parameters Inverted From the Compaction Experiments on Mt. Gambier Limestone

Parameter	Diffuse band	Discrete band array	Units
$\mathcal{G}_c$	8×10^{-7}	8×10^{-7}	m/s
L	2.4	2.0	mm
r_d	0.59	0.5	-

different pattern evolution rates, the simulation results were carefully compared with the experimental observations for the pattern formation matching. Figure 12 demonstrates the simulated diffuse band with the best fitting performance, and the corresponding regularization parameters are listed in Table 2. The evolution of the damage band is in good agreement with the porosity reduction profile, which suggests that the damageable MCC model is capable of capturing the formation of diffuse compaction bands arising from the microscopic processes such as pore collapse and grain crushing during the triaxial loading. Compared with the band evolution rate 8×10^{-5} m/s in Townend et al. (2008), the characteristic velocity $\mathcal{G}_c$ inverted here is significantly smaller due to the different rock specimens used in experiments, that is, the specimens used by Townend et al. (2008) are sandstones which are more homogeneous and less porous while here we used limestone samples.

It needs to be noted that each X-ray scan in the above experiments takes around 1 hr, resulting in limited time resolution for the observation of pattern formation. To mitigate this limitation, supplementary compaction experiments were performed using the digital image correlation (DIC) technique providing a real-time measurement of the specimen deformation. But different from the above-described X-ray transparent triaxial loading cell, the supplementary experiments were conducted using an optically transparent oedemetric setup, where the Mt. Gambier limestone sample was placed in a thick-walled acrylic tube to mimick an oedemetric loading condition for soft rocks under compaction loading. The limestone sample was wrapped in a transparent membrane with negligible thickness and Teflon spay was applied to eliminate the side friction between the sample and the interior of the cylindrical chamber.

Figure 13 presents the DIC analysis results on the compressive strain distribution in the experiments. A tabular compaction band, which may be triggered by a locally concentrated porosity increase, appeared first in the upper portion of the sample. As the compaction loading continued, the first band grew in thickness and more bands emerged in the highly porous limestone sample, comprising an array of discrete compaction bands. To reproduce the band array numerically, we chose parameters from Zone 2 in Figure 11 for the simulation. In this procedure, an initial damage seed was imposed (similar in size as shown in Figure 8a) at the location where the first band was observed from the DIC analysis, for the nucleation of the simulated band. The simulated results with the best fitting performance are displayed next to the experimental results in Figure 13. The simulated damage distribution pattern well matches the experimental observations in terms of both the band width and the band spacing. Certain discrepancy on the band close to the bottom plate appeared, which is mainly due to the fact that the numerical experiment assumes an idealized boundary condition while in laboratory experiments there are shear offsets occurring in the near-boundary region. The corresponding regularization parameters are also listed in Table 2, with the same value of $\mathcal{G}_c$ used for simulating the diffusive band growth within the Mt. Gambier Limestone sample shown in Figure 12.

4. Discussion

The present manuscript was motivated by providing an analysis technique for the recent observation of compaction bands in highly porous carbonates where a rich family of compaction localisation features was observed. Of particular interest was trying to understand the reasoning for a transition from a mode of discrete compaction band formation to a diffuse compaction band growth. The current numerical approaches have so far only described the formation of discrete bands and the growth of diffuse bands was not yet available. Recent progress on the numerical formulations for compaction band growth (Ip & Borja, 2022; Wang et al., 2023) has overcome the inherent problem of mesh sensitivity of earlier numerical solutions by using a phase field approach, however, the diffusive growth mode was not described. We have developed an alternative solution to overcome the mesh-sensitivity by extending a thermodynamic approach (Jacquey & Regenauer-Lieb, 2021) with a newly developed reaction-diffusion formalism. In this approach we have considered an additional entropy flux (Regenauer-Lieb & Hu, 2023) that can regularize the solution through a characteristic diffusion length scale. The addition of this new parameter not only solved the mesh-dependency of the original thermodynamically based formulation but led to a richer solution space of compaction bands including the diffuse mode.

The consideration of non-local models follows a long tradition, introduced for the problem considered here, by Triantafyllidis and Aifantis (1986) who first captured post-localisation features such as deformation band width

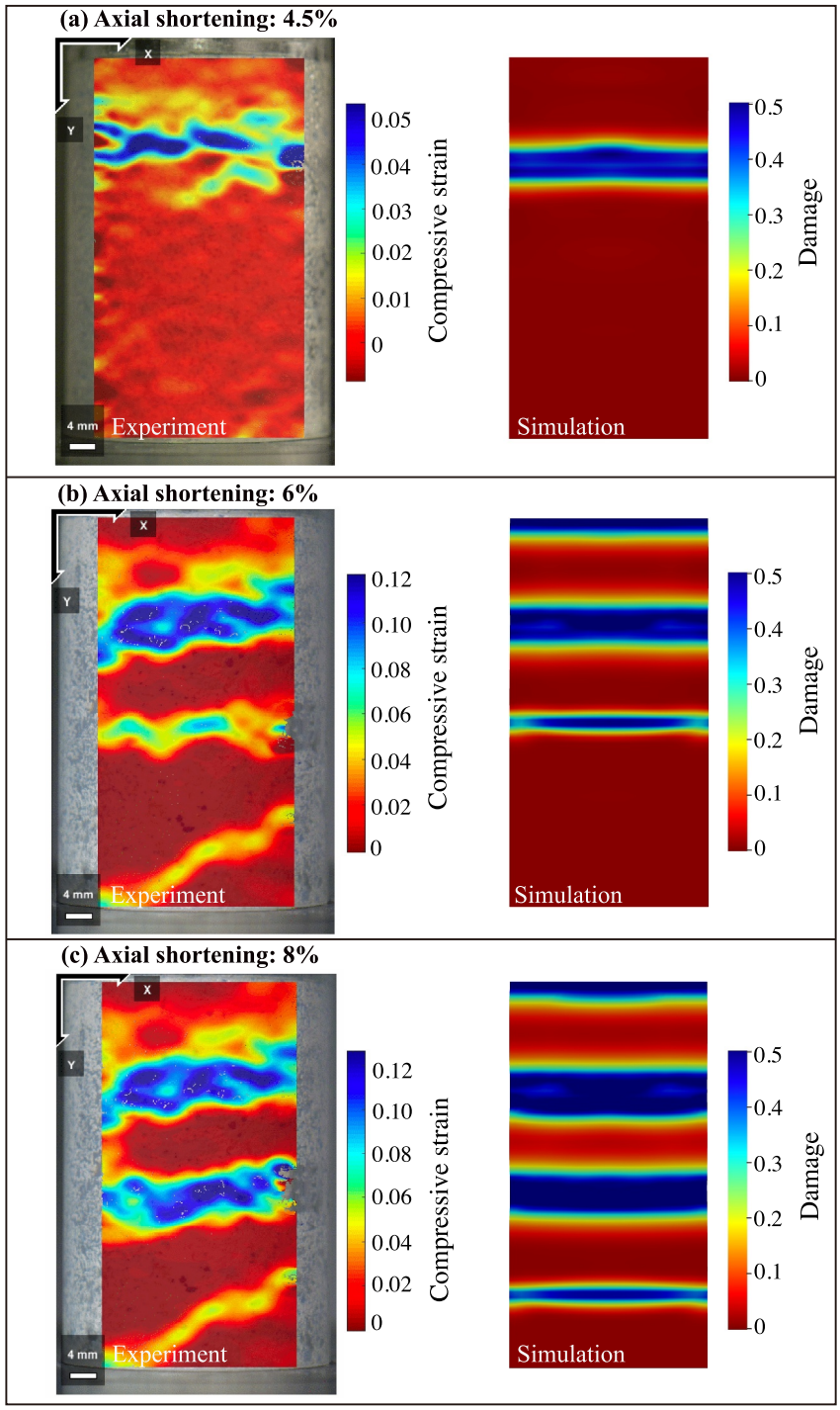

Figure 13. Discrete compaction band arrays in Mt. Gambier Limestone samples. The left panel shows the compressive strain pattern via digital image correlation analysis and the right panel is the simulated damage band patterns. The first compaction band observed in experiments is considered as being triggered by a heterogeneity effect which is mimicked in the numerical tests by applying an initial damage seed in the specimen.

by including higher-order deformation gradients into the strain energy function. Similarly, the theory of critical distances (Taylor, 2007) overcame the limitation of linear elastic fracture mechanics on capturing important features of the physical mechanism of cracking processes through acknowledgment of mechanisms at the microstructural level, represented by the introduction of a single length scale parameter. The recognition of these

discrete features connected through a cascade of length scales in a hierarchical network of faults and fractures has been used to reveal the critical point phenomena through the self-similarity of the Gutenberg-Richter relationship of earthquakes (Naimark, 2008). The model presented here is a thermodynamics-inspired approach sharing resemblance with the original work of Lyakhovsky et al. (2011) for damageable materials but further incorporates a recent postulate of an entropic velocity which is a characteristic of the dynamic interactions at microstructural level in generic solid-like materials (Regenauer-Lieb & Hu, 2023).

The consideration of a new diffusion formulation of the damage zone which regularizes the growth of the compaction band is described by the parameter $\mathcal{G}_c$, the entropic velocity of the compaction band that also controls the newly identified dynamic equilibrium diffusion length scale l interpreted as the maximum entropy density of the state towards which the compaction band is equilibrating (Regenauer-Lieb & Hu, 2023). The consideration of an entropic flux at the scale of compaction bands can be derived directly from the dynamic interaction of the two phases which are in the described limestone experiment the intact matrix and the crushed grains (Regenauer-Lieb & Hu, 2023). The entropic velocity stems from the interactions of a granular medium where the crushed grains follow the path of the least resistance in the energy landscape during the minimization of the free energy, as the compaction process proceeds, thus ensuring maximum entropy production in the dissipation process. If the parameter $\mathcal{G}_c$ is large it promotes the formation of discrete compaction bands because together with the introduced dynamic equilibrium length scale l it regularizes the solution by compensating the source term r_d. For negligible $\mathcal{G}_c$ the regularization collapses and the mesh sensitivity problem is encountered. The entropic velocity $\mathcal{G}_c$ is a characteristic rate quantity controlling the speed of the compaction band formation process which is directly measurable in experiments.

Our new formulation is numerically robust and therefore also allows the investigation of the effect of material heterogeneities that can influence the growth of compaction bands. We have used this capability to replicate the areas of increased porosity recorded in the limestone experiment in Figure 13 which were found to nucleate the growth of the first compaction band in the experiment recorded by DIC. For the model of the diffuse compaction band growth shown by the CT-scan in Figure 12 we did not use a seed as the sample appeared to be homogenous and the band nucleated on the boundary.

Although we have in the current work tried to incorporate the microprocesses that are causing the compaction band formation through a damage mechanics formulation we would like to highlight the main limitation of our current approach. The nature of the formulation still relies on a macroscopic perspective which does not include the microphysics of the processes. The consideration of the entropic velocity is the only microphysical property that is present in the current formulation, however, the length scale l is still a geometrical constant and does not consider the stochastic nature of the discrete interactions of the deformation processes inside the compaction band but assumes that an equilibrium entropy density l exists towards which the state of the compaction band is equilibrating. This assumption is an extension of Onsager's microreversible principle to non-local dynamic equilibria and is discussed in a separate contribution where a physics-based approach is used to consider the interaction between the solid skeleton and the crushed grains stemming from the small scale (Regenauer-Lieb & Hu, 2023) thus allowing the consideration of the dynamic processes that trigger the nucleation and growth of compaction bands.

Finally, we note that the emphasis of this study is placed on visco-plastic failure modes, which are characteristically different from for example, elasto-dynamic failure in brittle materials. The material under consideration (see Figure A2) is a highly porous soft rock undergoing compaction with an application of confining pressure, which is expected to exhibit "stable fracturing", that is, the rate of damage accumulation slows down when damage approaches unity as Figure A2 illustrates, due to significant strain hardening. It is worth noting that during the stable fracturing stage the growth rate of the lateral displacement of the compacting specimen also decreases, supporting the mechanism of prominent pore collapse in the case of sufficiently high confinement. The presented model hence does not intend to represent general failure mechanisms of brittle rocks but captures the ductilization effect (a transition to ductile behavior occurring in porous rocks) enabled by confined compaction under room temperature condition.

5. Conclusion

In this work we have presented a stable numerical method which regularizes the width of compaction and shear bands using a thermodynamic perspective. The approach is in principle universally applicable to conditions in laboratory experiments as described in this work but it provides equally a novel analysis technique for the

deformation bands observed in field exposures. Under the assumption that these features constitute a stationary instability, the numerical method therefore allows inversion of material parameters from observation of band width and spacing considering the geometrical context of the width of the deformation and the length scale of the banding features. The novel parameter describing the entropic velocity of compaction band growth $\mathcal{G}_c$ is, however, only available through analysis of time series which restricts its derivation to the laboratory or geophysical observations of active fault zones.

Our new development has predicted a rich solution space including those not covered in classical compaction models, both for numerical solutions and solid mechanical theories. Laboratory experiments have described a class of diffuse compaction band growth which was not yet predicted by standard models or numerical experiments. We have proposed here a novel thermodynamics-inspired mechanism attempting to overcome the notorious numerical mesh size issues for band spacing and width. We note, that although in the present work we have focused on an analysis of compaction bands the formulation is generic and we hence expect a similar diffuse dilatant or compactive shear band growth as observed in our numerical experiments. The numerical code can be downloaded and further work for a systematic investigation of the formation of deformation bands in both nature and the laboratory in encouraged.

Appendix A

A1. Finite Element Formulation

The governing equations solved in the LEMUR simulator include the equilibrium of momentum and the evolution of damage. The damage evolution Equation 44 has been introduced in the main text, while the momentum equilibrium in the domain $\mathcal{B}$ with boundary $\partial\mathcal{B}$ takes the form

$$\begin{cases} \nabla\cdot\boldsymbol{\sigma}+\rho\boldsymbol{g}=\boldsymbol{0} & \text{in} \quad \mathcal{B} \\ \boldsymbol{n}\cdot\boldsymbol{\sigma}=\bar{\boldsymbol{t}} & \text{on} \quad \partial\mathcal{B}_t \\ \boldsymbol{u}=\bar{\boldsymbol{u}} & \text{on} \quad \partial\mathcal{B}_u \end{cases} \tag{A1}$$

where $\boldsymbol{\sigma}$ is the Cauchy stress, $\rho\boldsymbol{g}$ is the body force, $\boldsymbol{n}$ represents the unit normal vector to the boundary $\partial\mathcal{B}_t$ where the surface traction $\bar{\boldsymbol{t}}$ is prescribed, and $\bar{\boldsymbol{u}}$ is the prescribed displacement on the boundary $\partial\mathcal{B}_u$.

Define the weighting functions $\boldsymbol{\eta}\in\mathcal{V}$ and $\phi\in\mathcal{W}$, which belong in the appropriate sets $\mathcal{V}$ and $\mathcal{W}$, respectively. The weak form of the governing equations can be written as.

$$\int_{\mathcal{B}}\boldsymbol{\eta}\cdot(\nabla\cdot\boldsymbol{\sigma}+\rho\boldsymbol{g})\mathrm{d}V=0 \tag{A2a}$$

$$\int_{\mathcal{B}}\phi\cdot\left[\dot{\alpha}_d-\mathcal{G}_c\left(l\nabla^2\alpha_d-\frac{\alpha_d}{l}\right)-\frac{\left(r_s^2+r_d^2\right)\pi}{r_v^2\bar{\chi}_d}\dot{\varepsilon}_v^p-\frac{\left(r_v^2+r_d^2\right)\chi}{r_s^2\bar{\chi}_d}\dot{\gamma}^p\right]=0 \tag{A2b}$$

Integrating by parts with the use of divergence theorem, the following variational equations for the momentum equilibrium and damage evolution can be obtained.

$$\int_{\mathcal{B}}\nabla^s\boldsymbol{\eta}:\boldsymbol{\sigma}\mathrm{d}V-\int_{\mathcal{B}}\boldsymbol{\eta}\cdot\rho\boldsymbol{g}\mathrm{d}V-\int_{\partial\mathcal{B}_t}\boldsymbol{\eta}\cdot\bar{\boldsymbol{t}}\mathrm{d}A=0 \tag{A3a}$$

$$\int_{\mathcal{B}}\phi\dot{\alpha}_d\mathrm{d}V+\int_{\mathcal{B}}\mathcal{G}_c\left(l\nabla\phi\cdot\nabla\alpha_d+\phi\frac{\alpha_d}{l}\right)\mathrm{d}V-\int_{\mathcal{B}}\phi\left(\frac{\left(r_s^2+r_d^2\right)\pi}{r_v^2\bar{\chi}_d}\dot{\varepsilon}_v^p+\frac{\left(r_v^2+r_d^2\right)\chi}{r_s^2\bar{\chi}_d}\dot{\gamma}^p\right)\mathrm{d}V=0 \tag{A3b}$$

Where $\nabla^s=(\nabla+\nabla^T)/2$ denotes the symmetric gradient operator. In the LEMUR simulator, the variational equations are implemented via the kernel module based on the MOOSE framework (Permann et al., 2020). For Equation A3a, a stress divergence kernel which relies on the stress update procedure as described in the main text is used to ensure the momentum equilibrium, while a damage evolution kernel is utilized for implementing Equation A3b. In the damage kernel, a backwards-Euler scheme is adopted to tackle the first integral term in

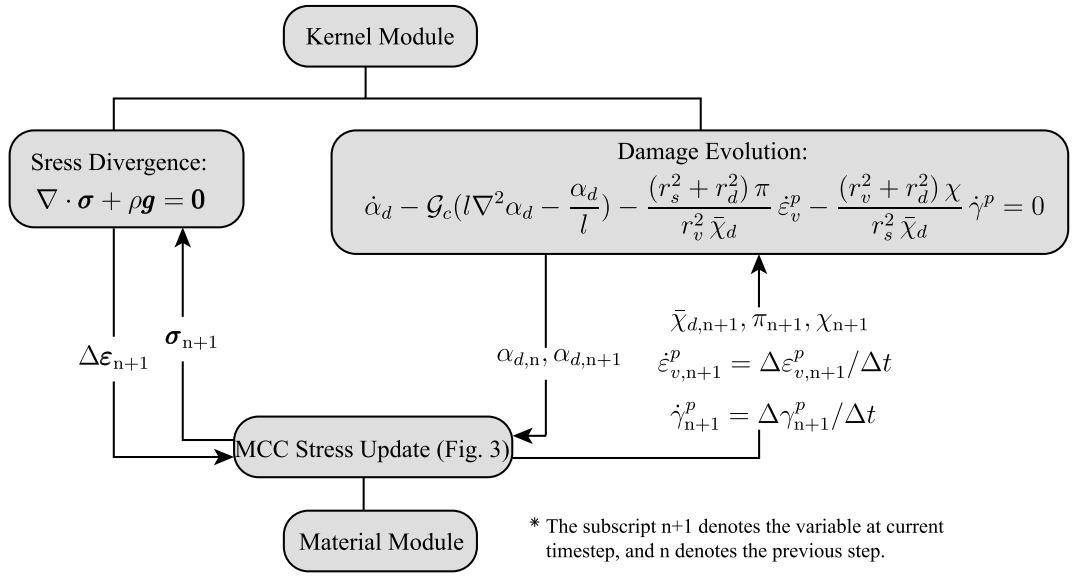

Figure A1. Interaction between the kernel and material modules in the LEMUR simulator.

Equation A3b, whereas the remaining regularized damage source needs to couple the stress and strain information from the stress update procedure in the material module. Such coupled interaction between the kernel and material modules is illustrated in Figure A1, along with the corresponding governing equations (strong form to simplify notation).

A2. Damage Evolution via Single-Element Test

As demonstrated by Equation 44, the damage accumulation is dependent on the deformation conditions as well as the dissipation splitting coefficients. Here, single-element tests are performed to illustrate representative damage evolution during the compaction process. Given the non-local nature of the regularized terms in Equation 44, $\mathcal{G}_c$ is

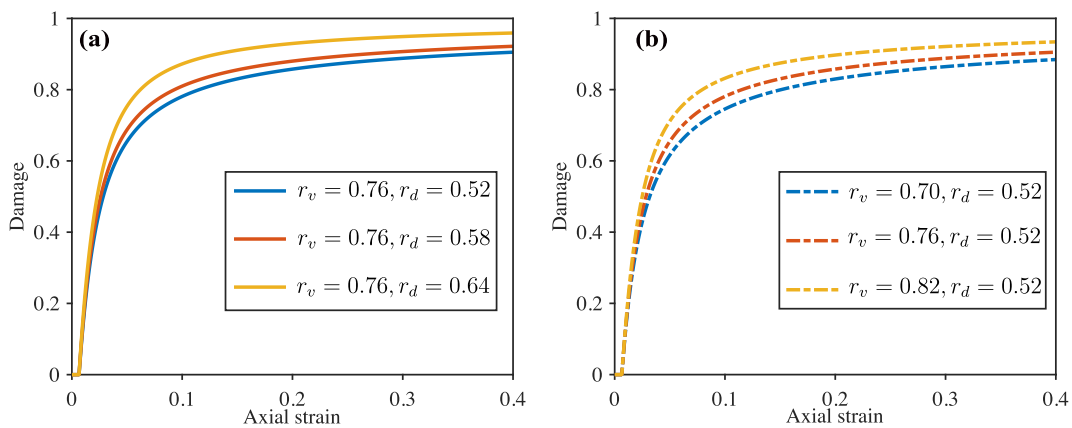

Figure A2. Damage evolution in highly porous rock samples (under confining pressure of 5 MPa) via single-element tests.

set as 0 to facilitate the single-element analysis. The results in Figure A2 indicate that the change of either the dissipation splitting coefficient r_d or r_v may alter the damage source terms in Equation 44, thus leading to damage value variation at a given loading strain. Moreover, the damage rate of all curves in Figure A2 decreases with the growth of the damage value. This is because by substituting Equation 21 into Equation 44, the last two damage source terms are close to 0 as damage approaches to 1, resulting in vanishing damage increment in this case.

A3. Rate-Dependent Flow Rules

The flow rules in the main text are formulated in a rate-independent manner. Here, we extend the constitutive laws to take into account the rate-dependent effects. To derive the visco-plasticity model, we still make use of the thermomechanics framework (Collins, 2003), assuming a dissipation function of the following form

$$\hat{\Phi} = \sqrt{\left(A\dot{\varepsilon}_v^p\right)^2 + \left(B\dot{\gamma}^p\right)^2} + \frac{1}{2}\eta\left[\left(A\dot{\varepsilon}_v^p\right)^2 + \left(B\dot{\gamma}^p\right)^2\right] \tag{A4}$$

where η has the dimension of the inverse of the dissipation function, that is, $\mathrm{Pa}^{-1}\cdot\mathrm{s}$. The dissipative stress invariants can still be defined as the derivatives of the above dissipation function.

$$\pi = \frac{\partial\hat{\Phi}}{\partial\dot{\varepsilon}_v^p} = \frac{A^2\dot{\varepsilon}_v^p}{\sqrt{\left(A\dot{\varepsilon}_v^p\right)^2 + \left(B\dot{\gamma}^p\right)^2}} + \eta A^2\dot{\varepsilon}_v^p = \eta\frac{\sqrt{\left(A\dot{\varepsilon}_v^p\right)^2 + \left(B\dot{\gamma}^p\right)^2 + 1}}{\sqrt{\left(A\dot{\varepsilon}_v^p\right)^2 + \left(B\dot{\gamma}^p\right)^2}}A^2\dot{\varepsilon}_v^p \tag{A5a}$$

$$\chi = \frac{\partial\hat{\Phi}}{\partial\dot{\gamma}^p} = \frac{B^2\dot{\gamma}^p}{\sqrt{\left(A\dot{\varepsilon}_v^p\right)^2 + \left(B\dot{\gamma}^p\right)^2}} + \eta B^2\dot{\gamma}^p = \eta\frac{\sqrt{\left(A\dot{\varepsilon}_v^p\right)^2 + \left(B\dot{\gamma}^p\right)^2 + 1}}{\sqrt{\left(A\dot{\varepsilon}_v^p\right)^2 + \left(B\dot{\gamma}^p\right)^2}}B^2\dot{\gamma}^p \tag{A5b}$$

Which can lead to.

$$\dot{\varepsilon}_v^p = \frac{\pi}{A^2}\frac{\sqrt{\left(A\dot{\varepsilon}_v^p\right)^2 + \left(B\dot{\gamma}^p\right)^2}}{1 + \eta\sqrt{\left(A\dot{\varepsilon}_v^p\right)^2 + \left(B\dot{\gamma}^p\right)^2}} \tag{A6a}$$

$$\dot{\gamma}^p = \frac{\chi}{B^2}\frac{\sqrt{\left(A\dot{\varepsilon}_v^p\right)^2 + \left(B\dot{\gamma}^p\right)^2}}{1 + \eta\sqrt{\left(A\dot{\varepsilon}_v^p\right)^2 + \left(B\dot{\gamma}^p\right)^2}} \tag{A6b}$$

Substituting the above expressions into the first term on the RHS of Equation A4, one can obtain the following identity

$$\sqrt{\left(A\dot{\varepsilon}_v^p\right)^2 + \left(B\dot{\gamma}^p\right)^2} = \frac{\left\langle\sqrt{\frac{\pi^2}{A^2} + \frac{\chi^2}{B^2}} - 1\right\rangle}{\eta} = \frac{\langle\mathcal{F}\rangle}{\eta} \tag{A7}$$

from which the yield function in the dissipative stress space can be identified $\mathcal{F} = \sqrt{\frac{\pi^2}{A^2} + \frac{\chi^2}{B^2}} - 1$. Note that $\langle\cdot\rangle := (\cdot + |\cdot|)/2$ are the Macaulay brackets, which can ensure the left term of Equation A7 is either null or positive. With the above equality, the flow rules for the plastic strain rates as shown in Equation A6 can be rewritten as follows.

$$\dot{\varepsilon}_v^p = \frac{\langle\mathcal{F}\rangle}{\eta(1+\mathcal{F})}\frac{\pi}{A^2} = \frac{\langle\mathcal{F}\rangle}{\eta}\frac{\partial\mathcal{F}}{\partial\pi} \tag{A8a}$$

$$\dot{\gamma}^p = \frac{\langle\mathcal{F}\rangle}{\eta(1+\mathcal{F})}\frac{\chi}{B^2} = \frac{\langle\mathcal{F}\rangle}{\eta}\frac{\partial\mathcal{F}}{\partial\chi} \tag{A8b}$$

The flow rules derived here are the rate-dependent end-member of the model, and the derivation procedure is in fact thermomechanics equivalent to the visco-plastic flow rules introduced by (Perzyna, 1966).

Data Availability Statement

The Finite Element Method code is available on Mendeley Data (Sun et al., 2023).

Acknowledgments
The authors thank Dr. Antoine B. Jacquey from Polytechnique Montreal for providing the LEMUR code and helpful discussion. The support of the Research Grant Council of Hong Kong (ECS 27203720 and GRF 17206521) and the Australian Research Council (ARC DP200102517, DP170104550, LP170100233) is acknowledged.

References

Abdallah, Y., Sulem, J., Bornert, M., Ghabezloo, S., & Stefanou, I. (2021). Compaction banding in high-porosity carbonate rocks: 1. Experimental observations. *Journal of Geophysical Research: Solid Earth*, *126*(1), e2020JB020538. https://doi.org/10.1029/2020JB020538

Abdallah, Y., Sulem, J., & Stefanou, I. (2020). Compaction banding in high-porosity carbonate rocks: 2. A gradient-dependent plasticity model. *Journal of Geophysical Research: Solid Earth*, *125*(12), e2020JB020610. https://doi.org/10.1029/2020JB020610

Alevizos, S., Poulet, T., Sari, M., Lesueur, M., Regenauer-Lieb, K., & Veveakis, M. (2017). A framework for fracture network formation in overpressurised impermeable shale: Deformability versus diagenesis. *Rock Mechanics and Rock Engineering*, *50*(3), 689–703. https://doi.org/10.1007/s00603-016-0996-y

Baxevanis, T., Papamichos, E., Flornes, O., & Larsen, I. (2006). Compaction bands and induced permeability reduction in tuffeau de maastricht calcarenite. *Acta Geotechnica*, *1*(2), 123–135. https://doi.org/10.1007/s11440-006-0011-y

Bigoni, D., & Hueckel, T. (1991). Uniqueness and localization—I. Associative and non-associative elastoplasticity. *International Journal of Solids and Structures*, *28*(2), 197–213. https://doi.org/10.1016/0020-7683(91)90205-T

Browning, J., Meredith, P. G., Stuart, C., Harland, S., Healy, D., & Mitchell, T. M. (2018). A directional crack damage memory effect in sandstone under true triaxial loading. *Geophysical Research Letters*, *45*(14), 6878–6886. https://doi.org/10.1029/2018GL078207

Cacace, M., & Jacquey, A. B. (2017). Flexible parallel implicit modelling of coupled thermal–hydraulic–mechanical processes in fractured rocks. *Solid Earth*, *8*(5), 921–941. https://doi.org/10.5194/se-8-921-2017

Chemenda, A. I. (2009). The formation of tabular compaction-band arrays: Theoretical and numerical analysis. *Journal of the Mechanics and Physics of Solids*, *57*(5), 851–868. https://doi.org/10.1016/j.jmps.2009.01.007

Chemenda, A. I., Ballas, G., & Soliva, R. (2014). Impact of a multilayer structure on initiation and evolution of strain localization in porous rocks: Field observations and numerical modeling. *Tectonophysics*, *631*, 29–36. https://doi.org/10.1016/j.tecto.2014.01.021

Chen, X., Regenauer-Lieb, K., Lv, A., Hu, M., & Roshan, H. (2020). The dynamic evolution of compaction bands in highly porous carbonates: The role of local heterogeneity for nucleation and propagation. *Progress in Earth and Planetary Science*, *7*(1), 1–19. https://doi.org/10.1186/s40645-020-00344-0

Chen, X., Regenauer-Lieb, K., Lv, A., Hu, M., & Roshan, H. (2020). The dynamic evolution of permeability in compacting carbonates: Phase transition and critical points. *Transport in Porous Media*, *135*(3), 687–711. https://doi.org/10.1007/s11242-020-01493-y

Chen, X., Regenauer-Lieb, K., & Roshan, H. (2022). Temperature-induced ductile–brittle transition in porous carbonates and change in compaction band growth revealed by 4-D X-Ray tomography. *Rock Mechanics and Rock Engineering*, *55*(3), 1087–1110. https://doi.org/10.1007/s00603-021-02736-0

Collins, I. (2002). Associated and non-associated aspects of the constitutive laws for coupled elastic/plastic materials. *International Journal of Geomechanics*, *2*(2), 259–267. https://doi.org/10.1080/15323640208500176

Collins, I. (2003). A systematic procedure for constructing critical state models in three dimensions. *International Journal of Solids and Structures*, *40*(17), 4379–4397. https://doi.org/10.1016/S0020-7683(03)00226-9

Collins, I., & Houlsby, G. (1997). Application of thermomechanical principles to the modelling of geotechnical materials. *Proceedings of the Royal Society of London. Series A: Mathematical, Physical and Engineering Sciences*, *453*, 1975–2001. https://doi.org/10.1098/rspa.1997.0107

Collins, I., & Kelly, P. (2002). A thermomechanical analysis of a family of soil models. *Géotechnique*, *52*(7), 507–518. https://doi.org/10.1680/geot.2002.52.7.507

Einav, I., & Collins, I. F. (2008). A thermomechanical framework of plasticity based on probabilistic micromechanics. *Journal of Mechanics of Materials and Structures*, *3*(5), 867–892. https://doi.org/10.2140/jomms.2008.3.867

Fossen, H., Soliva, R., Ballas, G., Trzaskos, B., Cavalcante, C., & Schultz, R. A. (2018). A review of deformation bands in reservoir sandstones: Geometries, mechanisms and distribution. *Geological Society, London, Special Publications*, *459*(1), 9–33. https://doi.org/10.1144/sp459.4

Hill, R. (1962). Acceleration waves in solids. *Journal of the Mechanics and Physics of Solids*, *10*(1), 1–16. https://doi.org/10.1016/0022-5096(62)90024-8

Holcomb, D., Rudnicki, J. W., Issen, K. A., & Sternlof, K. (2007). Compaction localization in the earth and the laboratory: State of the research and research directions. *Acta Geotechnica*, *2*, 1–15. https://doi.org/10.1007/s11440-007-0027-y

Houlsby, G., & Puzrin, A. (2007). *Principles of hyperplasticity: An approach to plasticity theory based on thermodynamic principles*. Springer Science and Business Media.

Hu, M., Veveakis, M., Poulet, T., & Regenauer-Lieb, K. (2017). The role of temperature in shear instability and bifurcation of internally pressurized deep boreholes. *Rock Mechanics and Rock Engineering*, *50*(11), 3003–3017. https://doi.org/10.1007/s00603-017-1291-2

Huang, L., Baud, P., Cordonnier, B., Renard, F., Liu, L., & Wong, T.-f. (2019). Synchrotron X-ray imaging in 4D: Multiscale failure and compaction localization in triaxially compressed porous limestone. *Earth and Planetary Science Letters*, *528*, 115831. https://doi.org/10.1016/j.epsl.2019.115831

Ip, S. C. Y., & Borja, R. I. (2022). A phase-field approach for compaction band formation due to grain crushing. *International Journal for Numerical and Analytical Methods in Geomechanics*, *46*(16), 2965–2987. https://doi.org/10.1002/nag.3436

Jacquey, A. B., Rattez, H., & Veveakis, M. (2021a). Strain localization regularization and patterns formation in rate-dependent plastic materials with multiphysics coupling. *Journal of the Mechanics and Physics of Solids*, *152*, 104422. https://doi.org/10.1016/j.jmps.2021.104422

Jacquey, A. B., & Regenauer-Lieb, K. (2021). Thermomechanics for geological, civil engineering and geodynamic applications: Rate-dependent critical state line models. *Rock Mechanics and Rock Engineering*, *54*(10), 5355–5373. https://doi.org/10.1007/s00603-021-02397-z

Jacquey, A. B., Regenauer-Lieb, K., & Cacace, M. (2021). Thermomechanics for geological, civil engineering and geodynamic applications: Numerical implementation and application to the Bentheim sandstone. *Rock Mechanics and Rock Engineering*, *54*(10), 5337–5354. https://doi.org/10.1007/s00603-021-02582-0

Kurzon, I., Lyakhovsky, V., & Ben-Zion, Y. (2021). Earthquake source properties from analysis of dynamic ruptures and far-field seismic waves in a damage-breakage model. *Geophysical Journal International*, *224*(3), 1793–1810. https://doi.org/10.1093/gji/ggaa509

Lyakhovsky, V., Hamiel, Y., & Ben-Zion, Y. (2011). A non-local visco-elastic damage model and dynamic fracturing. *Journal of the Mechanics and Physics of Solids*, *59*(9), 1752–1776. https://doi.org/10.1016/j.jmps.2011.05.016

Mir, A., Nguyen, G. D., & Sheikh, A. H. (2018). A thermodynamics-based model for brittle to ductile behaviour and localised failure of porous rocks. *International Journal of Solids and Structures*, *152*, 161–184. https://doi.org/10.1016/j.ijsolstr.2018.06.025

Mühlhaus, H. B., & Aifantis, E. C. (1991). A variational principle for gradient plasticity. *International Journal of Solids and Structures*, *28*(7), 845–857. https://doi.org/10.1016/0020-7683(91)90004-Y

Mühlhaus, H. B., & Vardoulakis, I. (1987). The thickness of shear bands in granular materials. *Géotechnique*, *37*(3), 271–283. https://doi.org/10.1680/geot.1987.37.3.271

Naimark, O. B. (2008). Structural-scaling transitions and self-similar features of earthquake development. *Physical Mesomechanics*, *11*(3), 187–201. https://doi.org/10.1016/j.physme.2008.07.008

Permann, C. J., Gaston, D. R., Andrš, D., Carlsen, R. W., Kong, F., Lindsay, A. D., et al. (2020). Moose: Enabling massively parallel multiphysics simulation. *SoftwareX*, *11*, 100430. https://doi.org/10.1016/j.softx.2020.100430

Perzyna, P. (1966). Fundamental problems in viscoplasticity. *Advances in Applied Mechanics*, *9*, 243–377. https://doi.org/10.1016/S0065-2156(08)70009-7

Poulet, T., Paesold, M., & Veveakis, M. (2017). Multi-physics modelling of fault mechanics using redback: A parallel open-source simulator for tightly coupled problems. *Rock Mechanics and Rock Engineering*, *50*(3), 733–749. https://doi.org/10.1007/s00603-016-0927-y

Rattez, H., Stefanou, I., Sulem, J., Veveakis, M., & Poulet, T. (2018). The importance of thermo-hydro-mechanical couplings and microstructure to strain localization in 3d continua with application to seismic faults. Part II: Numerical implementation and post-bifurcation analysis. *Journal of the Mechanics and Physics of Solids*, *115*, 1–29. https://doi.org/10.1016/j.jmps.2018.03.003

Regenauer-Lieb, K., & Hu, M. (2023). Emergence of precursor instabilities in geo-processes: Insights from dense active matter. *Heliyon*, *9*(12), e22701. https://doi.org/10.1016/j.heliyon.2023.e22701

Rice, J. R. (1976). The localization of plastic deformation. In W. T. Koiter (Ed.), *Theoretical and applied mechanics* (pp. 207–220). North-Holland.

Rudnicki, J. W., & Rice, J. (1975). Conditions for the localization of deformation in pressure-sensitive dilatant materials. *Journal of the Mechanics and Physics of Solids*, *23*(6), 371–394. https://doi.org/10.1016/0022-5096(75)90001-0

Simo, J. C., & Hughes, T. J. (2006). *Computational inelasticity* (Vol. 7). Springer Science and Business Media.

Stathas, A., & Stefanou, I. (2022). The role of viscous regularization in dynamical problems, strain localization and mesh dependency. *Computer Methods in Applied Mechanics and Engineering*, *388*, 114185. https://doi.org/10.1016/j.cma.2021.114185

Stefanou, I., & Gerolymatou, E. (2019). Strain localization in geomaterials and regularization: Rate-dependency, higher order continuum theories and multi-physics. *ALERT Doctoral School*, *780*, 47–85.

Sulem, J., & Vardoulakis, I. (1995). *Bifurcation analysis in geomechanics*. CRC Press.

Sun, Q., Chen, X., Regenauer-Lieb, K., & Hu, M. (2023). LEMUR solver with damage regularisation for deformation band study. [Dataset]. Mendeley Data. https://doi.org/10.17632/z69j8yxfzp.1

Tang, X., & Hu, M. (2023). Chemo-hydro-mechanics in a reactive rock under cylindrical fluid pressurization. *Computers and Geotechnics*, *162*, 105637. https://doi.org/10.1016/j.compgeo.2023.105637

Taylor, D. (2007). Chapter 13 - Theoretical aspects. [Book Section]. In D. Taylor (Ed.), *The theory of critical distances* (pp. 261–275). Elsevier Science Ltd. https://doi.org/10.1016/B978-008044478-9/50014-4

Townend, E., Thompson, B. D., Benson, P. M., Meredith, P. G., Baud, P., & Young, R. P. (2008). Imaging compaction band propagation in diemelstadt sandstone using acoustic emission locations. *Geophysical Research Letters*, *35*(15). https://doi.org/10.1029/2008GL034723

Triantafyllidis, N., & Aifantis, E. C. (1986). A gradient approach to localization of deformation. I. hyperelastic materials. *Journal of Elasticity*, *16*(3), 225–237. https://doi.org/10.1007/bf00040814

Veveakis, E., & Regenauer-Lieb, K. (2015). Cnoidal waves in solids. *Journal of the Mechanics and Physics of Solids*, *78*, 231–248. https://doi.org/10.1016/j.jmps.2015.02.010

Wang, Y., Borja, R. I., & Wu, W. (2023). Dynamic strain localization into a compaction band via a phase-field approach. *Journal of the Mechanics and Physics of Solids*, *173*, 105228. https://doi.org/10.1016/j.jmps.2023.105228

Wong, T.-f., & Baud, P. (2012). The brittle-ductile transition in porous rock: A review. *Journal of Structural Geology*, *44*, 25–53. https://doi.org/10.1016/j.jsg.2012.07.010

Zhao, J., Sheng, D., & Collins, I. (2006). Thermomechanical formulation of strain gradient plasticity for geomaterials. *Journal of Mechanics of Materials and Structures*, *1*(5), 837–863. https://doi.org/10.2140/jomms.2006.1.837